TWIST

Journal homepage: www.twistjournal.net

Current Advances in Biological Activities of New Metal Complexes Bearing Aromatic Hydroxy Schiff-base Ligand

Shaimaa Mohamed Faheem
Higher Technological Institute of Applied Health Sciences, Badr Academy, Badr City, Egypt

Abdou Saad El-Tabl
Department of Chemistry, Faculty of Science, El-Menoufia University, Shebin El -Kom, Egypt

Moshira Mohamed Abd-El Wahed
Department of Pathology, Faculty of Medicine, El-Menoufia University, Shebin El-Kom, Egypt

Mohammed Kaid*
Department of Chemistry, Faculty of Science, El-Menoufia University, Shebin El -Kom, Egypt
[*Corresponding author]

Sara M. Younes
Chemical Engineering Department, Borg El Arab Higher Institute Engineering and Technology, Alexandria, Egypt

Abstract

Metal complexes with biological activities are gaining prominence in the field of medicine as potential alternatives to biologically active organic compounds. These complexes possess distinctive characteristics, including molecular geometries not easily accessible by organic molecules and the ability to undergo ligand exchange, redox, catalytic, and photophysical reactions. These unique features provide the complexes with the potential to interact with biomolecules in unconventional ways and through distinct mechanisms of action.In light of these characteristics, we synthesized complexes with Cr(III), Mn(II), Fe(III), Ni(II), Co(II), Cu(II), Zn(II), Cd(II), Hg(II), Sn(II), and Ag(I) ions using the (E)-2-hydroxy-N-(2-((2-hydroxybenzylidene)amino)phenyl)benzamide ligand, a tetra-dentate Schiff-base. Characterization of the ligand and its complexes involved various techniques, including IR spectroscopy, elemental microanalysis, electronic spectra, magnetic susceptibility, conductivity, thermal analysis, proton nuclear magnetic resonance, mass spectroscopy, electron spin resonance, and electron microscopy. The proposed geometry for the complexes was an octahedral structure, with conductance measurements in DMF solution indicating non-electrolytic behavior.ESR measurements revealed anisotropic spectra with a $d(x^2-y^2)$ ground state and covalent bond character for Cu(II) complexes. In contrast, Cr(III), Fe(III), Mn(II), and Co(II) complexes exhibited isotropic types with an octahedral structure. Electron microscopic data suggested that the complexes existed in nano-form. The cytotoxicity ranking against HEPG-2 cell lines was Vinblastine Sulfate (standard) > Ag(I) complex(3) > Cd(II) complex (4) > Cu(II) complex (2) > Ligand (1). Molecular docking studies were also conducted for the compounds mentioned above.

INTRODUCTION

Schiff bases play a crucial role as chelating agents in the synthesis of transition metal complexes, whether they are mono-, di-, or polynuclear. Researchers have shown considerable interest in studying the synthesis, structure, and characteristics of Schiff-base complexes over the past two decades(Miyasaka et al., 1998). These complexes have been particularly intriguing due to their significant contributions to magnetism and material science, making them potential models for biologically relevant species(Correia et al., 2014, Dörr and Meggers, Li et al., 2014).The amide bond, a common chemical bond found in various organic compounds and biomolecules, is known for its strong stability under diverse reaction

conditions(Pattabiraman and Bode, Kaspar and Reichert, 2013, Clayden, 2003, Brown and Boström, Schmitz, 2010, Brunton et al., 2015). This stability arises from the amide bond's propensity to form a resonant structure(Simon et al., 2000), imparting a double bond nature to the CO-N bond(Mujika et al., 2005, Kemnitz and Loewen, 2007, Wang and Cao, 2011). This resonance results in a planar shape, restricting free rotation around the CO-N bond and contributing to the 3D structures adopted by proteins and biomolecules(Smith and Hansen, 1998). The stability and unique characteristics of amide bonds have led to their exploitation in creating vital biomolecules.Despite the stability of amide bonds, various strategies have been proposed in the literature to activate them for reactions with different nucleophiles or electrophiles(Radzicka and Wolfenden, 1996). One such method involves the distortion of amide bonds, reducing their double bond nature and increasing susceptibility to chemical attacks(Arnau et al., 2006, Hoyer et al., 1990, Schepartz and Cuenoud, 1990). N-acyl-glutarimides and N,N-substituted amide bonds are examples of compounds that achieve maximum rotational inversion of the amide bond (Artacho et al., 2012, Bashore et al., 2003, Kim et al., 2016, Kirby et al., 2001, Kirby et al., 1998a, Kirby et al., 1998b, Sawosz et al., 2010, Tani and Stoltz, 2006), enhancing reactivity toward a broad range of nucleophiles and electrophiles(Meng and Szostak, 2015b, Meng and Szostak, 2015a, Meng and Szostak, 2016b, Meng and Szostak, 2016a, Shi et al., 2016, Shi and Szostak, 2016).Schiff bases, characterized by the presence of an azomethine group (>C=N) (Hie et al., 2015, Li and Zou, 2015), have garnered attention for their synthesis and characteristics. Their unique structure makes them versatile compounds with applications in nanotechnology and biomedical fields (Chakravorty, 1974, Fessenden and Fessenden, 1998). Copper nanoparticles (Cu NPs) have attracted significant interest due to their size- and shape-dependent optical, catalytic, and therapeutic capabilities (Kosinska et al., 2019). Functional Cu NPs, in particular, have demonstrated promising medicinal potential, inducing apoptosis through target-specific mechanisms. Copper complexes, including those in nano-form, show potent anticancer properties, inhibiting DNA (Beilner et al., 2020, Huang et al., 2020) replication and mitosis.In the context of liver and breast cancers, which pose significant threats to human life, the limitations and side effects of existing medications have prompted the exploration of new strategies. The preparation and study of metal complexes in nano-form offer a modern approach to treatment. These complexes, thoroughly analyzed through analytical and spectroscopic methods, present a promising avenue for future cancer treatment.Hepatocellular carcinoma (HCC) stands out as one of the most common and deadly cancers globally, with rising incidence and mortality rates (Bao et al., 2013, Sawosz et al., 2010).The limited therapy options for HCC patients are often attributed to late-stage diagnoses. Similarly, breast cancer, the second most common cancer worldwide and the leading cause of mortality in women in Egypt, necessitates innovative strategies for treatment (Yogesh et al., 2016). The preparation and analysis of metal complexes in nano-form offer hope for addressing the challenges posed by these dangerous cancers.

EXPERIMENTAL
Materials
The initial chemicals employed were of analytical grade and utilized without additional purification.

Physical and Spectroscopic Techniques
The ligand and its associated metal complexes were characterized through a series of techniques:
1. Elemental analyses (C, H, N, Cl, and M) were conducted at the Microanalytical Center Laboratory of Cairo University, Egypt.
2. The molar conductivity of metal complexes in dimethyl sulfoxide (DMSO) at a concentration of 10^{-3} M was determined at room temperature using a Bibby conductimeter MCI. The molar conductivity values were calculated using the following equation:

$$\Lambda_M = \frac{V \times K \times g}{Mw * \Omega}$$

where
ΛM = molar conductivity / $\Omega^{-1} cm^2 mol^{-1}$
V = volume of the complex solution (100 cm^3)
K = cell constant (0.92/ cm^{-1})
Mw = molecular weight of the complex
g = weight of the complex/g
Ω = resistance/Ω

1. Mass spectra were acquired using BRUKER 400 MHz spectrometers. Chemical shifts (ppm) are reported relative to TMS.
2. Thermal analyses (DTA and TGA) were conducted on a Shimadzu DT-30 thermal analyzer, spanning from room temperature to 800 ºC at a heating rate of 10 ºC/min.
3. 1H-NMR spectra were obtained using BRUKER 400 MHz spectrometers, with chemical shifts (ppm) reported relative to TMS.

4. IR spectra of the ligand and its metal complexes were measured using KBr discs with a Jasco FT/IR 300E Fourier-transform infrared spectrophotometer covering the range 400-4000 cm⁻¹.
5. Electronic spectra in the 200-900 nm region were recorded on a Perkin-Elmer 550 spectrophotometer.
6. Magnetic susceptibilities were determined at 25 ℃ via the Gouy method, using mercuric tetrathiocyanatocobaltate(II) as the magnetic susceptibility standard. Diamagnetic corrections were estimated from Pascal's constant (El-Tabl et al., 2010).
7. Magnetic moments were calculated using the equation:

$$\mu_{eff.} = 2.84\sqrt{\chi_M^{corr}.T}$$

$$\chi_M^{corr} = \chi_m - D$$

$$\chi_m = \chi_a * Mw$$
$$\chi_a = \left[2.086L(R-R^\circ)/(10^9 W)\right]$$

where:

    χ_a: mass susceptibility
    L: sample length in cm
    R: tube +sample reading
    R_o : the empty reading
    W: mass ;f the sample
    χ_m : molar susceptibility
    Mw: molar weight
    χ_n : corrected molar susceptibility
    D: diamagnetic correction
    μ_{eff} : effective magnetic moment
    T: room temperature in Kelvin

The theoretical effective magnetic moment value calculated using the equation:
$$\mu_{eff} = [n(n-+2)]1/2$$

For the interpretation of the number of unpaired electrons (n), diamagnetic corrections were implemented through the analysis of Pascal's constant. Electron Spin Resonance (ESR) spectra were captured using the BRUKER EMX EPR spectrometer located at the National Center for Radiation Research and Technology (NCRRT). DPPH served as the standard material.To characterize the colloidal suspension of the complexes in distilled water through Transmission Electron Microscopy (TEM), samples were prepared by depositing the colloids onto carbon-coated TEM grids. The liquid carrier was allowed to evaporate in the air, and the samples were subsequently examined using a JEOL 1230 transmission electron microscope operating at 120 kV(El Tabl et al., 2021).

Synthesis of the Ligand (1)
The ligand, (H3L) was prepared as follows:-
Salicylic acid (20.0 g, 0.13 mol) dissolved in 30 cm3 of ethyl alcohol was refluxed with continuous stirring for one hour in presence of five drops of conc.H2SO4. leave the product to cool at room temperature to give ethyl salicylate. Benzen - 1,2- diamine (29.0 g,0.26 mol) dissolved in 25 cm3 of ethyl alcohol in 1:1 molar ratio.The mixture was refluxed with stirring for 2 hours and then left to cool at room temperature ,filtered off the formed precipitate and leave it to dry at room temperature. The ethanolic solution of product (N-(2-amino phenyl)-2-hydroxybenzamide) (24.0g , 0.08 mol) was added to 2-hydroxybenzaldehyde (22.9g, 0.08 mol) (1:1) dissolved in 30 cm3 ethanol . The mixture was stirred and refluxed for another two hours at 70 ᴼ C, then left to cool to room temperature. The solid product was filtered off, then dried under vacuum over anhydrous CaCl₂ to give the ligand. Analytical data of the ligand are given in Table 1. Synthesis of the ligand is shown in scheme (1).
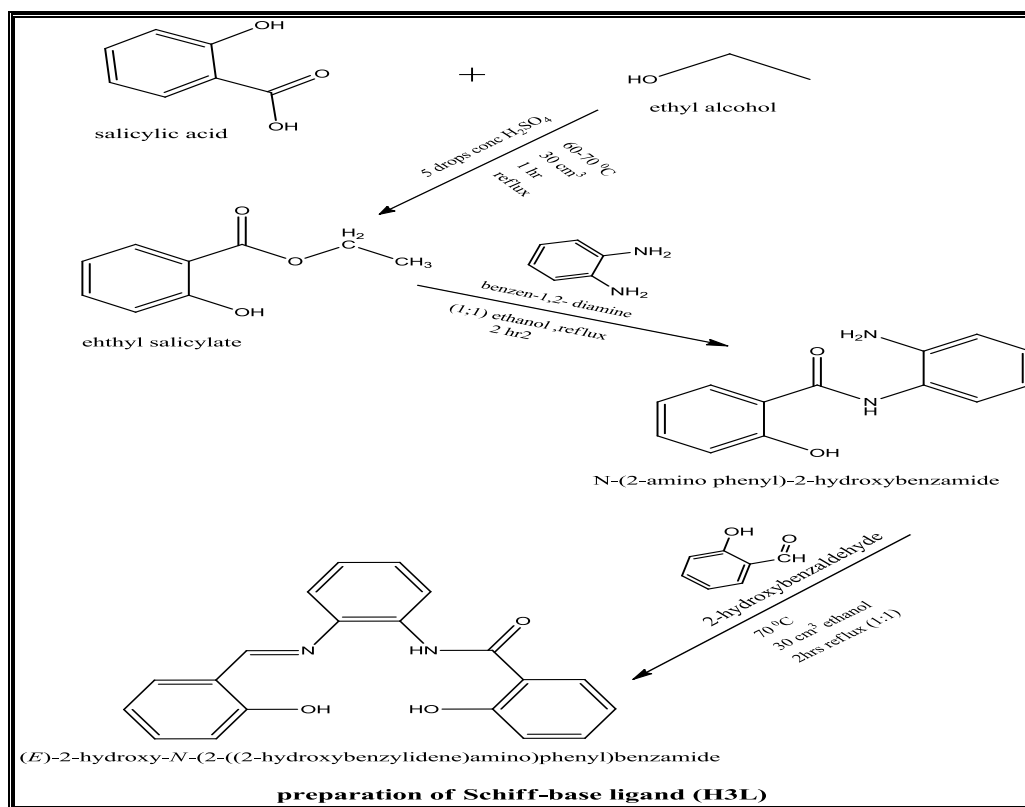
Scheme (1): Synthesis of of ligand **[H₁L] (1)**

Synthesis of Metal Complexes
Preparation of Metal Complexes, (2-4)

The Complexes were prepared by refluxing a hot ethanolic 30 cm³ solution of the ligand,(1) (1.01g, 0.003 mol) $CuCl_2.2 H_2O$, (1L:1M), complex (2) , (1.25 g, 0.003 mol) of Ag_2SO_4 (1L:1M), complex (3) , (1.54 g, 0.003 mol) of $CdCl_2.2 H_2O$ (1L:1M), complex (4) , The reaction mixtures were refluxed with stirring for 1–3 hrs range, depending on the nature of the metal ion and the anion. The precipitates so formed were filtrated off, washed with ethanol, and dried in desiccators over anhydrous $CaCl_2$.

BIOLOGICAL ACTIVITY
Cytotoxic Activity
1.   Material & Methods
1.1   Cell Culture and Treatment

The cell line, obtained from the National Cancer Institute, was maintained as a "monolayer culture" in RPMI medium supplemented with 10% FBS and 2% Pen/Strep. Cultures were incubated at 37 °C in 5% CO_2 within a high humidity environment using a water-jacketed incubator from Thermo Fisher Scientific USA. To ensure cells remained in the exponential growth phase, sub-culturing was routinely performed. Sterile conditions were maintained by conducting procedures in a laminar flow cabinet (Microflow Laminar flow cabinet, MDH limited, Hampshire SP105AA, U.K.). Experimental groups included a control group and treated groups exposed to varying drug concentrations (12.5, 25, 50, and 100 μg/mL).

1.2   Cell Proliferation Assay
1.   After the 24 h, add 10 μl of the MTT reagent (concentration 0.5 mg/ml) to each well.
2.   Incubate the microplate for 4 h.
3.   Add 100 μl of the solubilization solution into each well.
4.   After complete solubilization of the purple formazan crystals, measure the absorbance of the samples using a microplate (ELISA) reader. The wavelength to measure absorbance of the formazan product is570 nm.
The cell viability percentage was calculated using the following equation:
The cell viability (%) = [ODS/ ODC] × 100.
Where, ODS stands for the sample's mean optical density, while ODC is control's mean optical density. The results were displayed by a graph of percentage of cell viability versus the concentrations of the tested materials using Graphpad Prism 8.0.2. software.

2. Results and Discussion
All metal complexes exhibit vibrant colors and present as crystalline solids. These compounds possess non-hygroscopic properties and remain stable in the air at room temperature for an extended period, surpassing one year without

undergoing decomposition. The complexes demonstrate insolubility in various solvents such as water, ethanol, methanol, benzene, toluene, acetonitrile, and chloroform. However, they exhibit appreciable solubility in both dimethylformamide (DMF) and dimethylsulfoxide (DMSO). The analytical and physical data presented in Table 1, along with the spectral data in Tables 2-4, align well with the proposed structures depicted in Figure 1. Elemental analyses consistently indicate a 1:1 molar ratio for all complexes.

Table 1 Analytical and Physical Data of the Ligand [H$_3$L], (1) and its Metal complexes

No.	Ligands /Complexes	Color	FW	M.P (ºC)	Yield (%)	Analytical / Found calc.			Molar conductivity (Ohm^{-1}cm^{2}mol^{-1})
						C	H	N	
(1)	[H$_3$L]	Deep Brown	332	275 º C	75	P: 72.25 Th:72.3	P: 5.27 Th:4.81	P: 7.73 Th:8.43	2.11
(2)	[H$_3$L CuCl$_2$].2 H$_2$O	Brown	501	>300 º C	75	P:53.66 Th:53.69	P:4.27 Th:4.47	P:6.54 Th:6.26	7.3
(3)	[[H$_3$L Ag$_2$(SO$_4$)]	Black/Brown	642	>300 º C	70	P:36.79 Th:37.2	P:2.39 Th:2.48	P:4.88 Th:4.34	5.8
(4)	[H$_3$L CdCl$_2$].2 H$_2$O	Brown	552	>300 º C	72	Th:43.56	Th:3.63	Th:5.08	4.8

*Λm(Ω^{-1}cm^{2}mo^{-1})
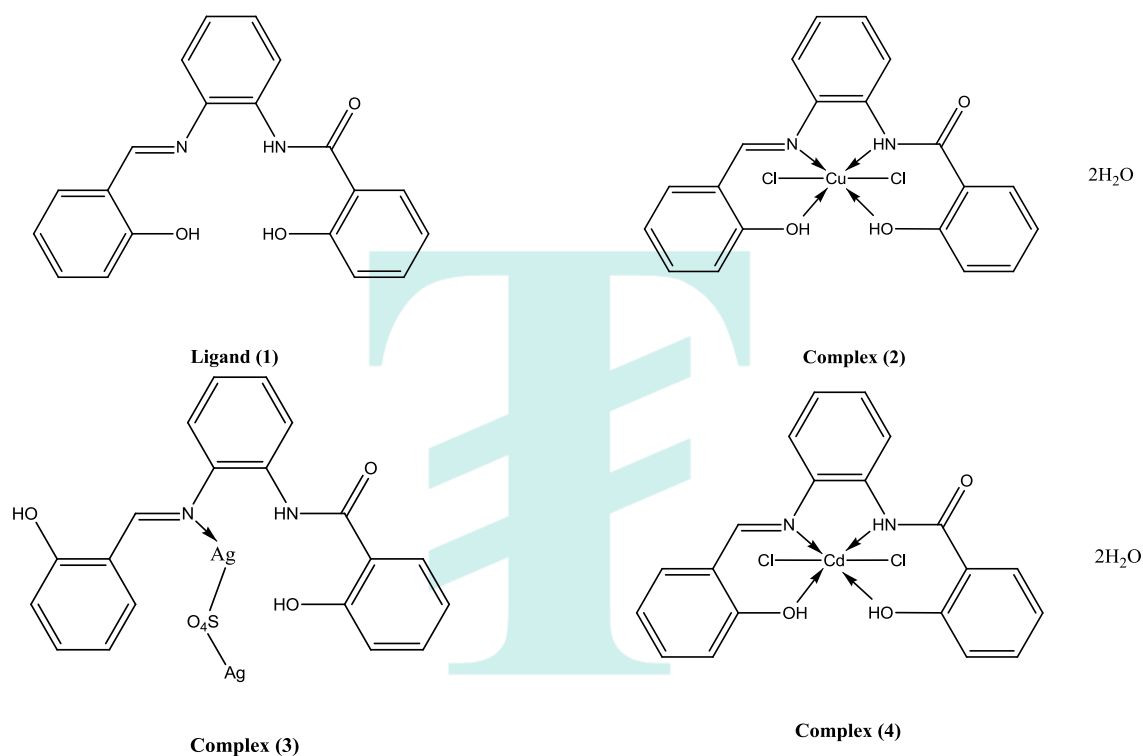
Figure 1 Proposed structures of the ligand and its metal complexes

CONDUCTANCE MEASUREMENTS

The molar conductivities of the complexes were determined in DMSO (1.0×10^-3 M). The recorded low magnitudes, as listed in Table 1, signify the non-electrolytic nature of all the complexes (El-Tabl et al., 2008). These values align well with the analytical data, indicating the involvement of anions groups in metal coordination.To confirm the molecular ion peaks of H3L and investigate fragment species, mass spectrometry was employed (Vogel, 1961). The spectrum of H3L displayed a molecular ion peak at m/z 332 amu, confirming its formula weight (F.W. 332) and the purity of the ligand. Notable mass fragmentation peaks observed at m/z = 52, 68, 76, 93, 106, 120, 136, 145, 158, 184, 211, 226, 280, 293, 315, 316, and 332 amu, corresponding to C$_4$H$_4$, C$_4$H$_4$O, C$_6$H$_4$, C$_6$H$_5$O, C$_7$H$_6$O, C$_7$H$_6$NO, C$_7$H$_6$NO$_2$, C$_9$H$_7$NO, C$_{10}$H$_8$NO, C$_{12}$H$_{10}$NO, C$_{13}$H$_{11}$N$_2$O, C$_{13}$H$_{10}$N$_2$O$_2$, C$_{16}$H$_{12}$N$_2$O$_3$, C$_{17}$H$_{13}$N$_2$O$_3$, C$_{20}$H$_{15}$N$_2$O$_3$, C$_{20}$H$_{16}$N$_2$O$_2$, and C$_{20}$H$_{16}$N$_2$O$_3$ moieties, respectively, strongly support the proposed structure of the ligand (Table 2,i).

Table 2 (i) Mass spectrum of the ligand [H$_3$L](**1**)

m/z	Rel. Int.	Fragment
52		C$_4$H$_4$
68		C$_4$H$_4$O
76		C$_6$H$_4$
93		C$_6$H$_5$O
106		C$_7$H$_6$O
120		C$_7$H$_6$NO

136	$C_7H_6NO_2$
145	C_9H_7NO
158	$C_{10}H_8NO$
184	$C_{12}H_{10}NO$
211	$C_{13}H_{11}N_2O$
226	$C_{13}H_{10}N_2O_2$
280	$C_{16}H_{12}N_2O_3$
293	$C_{17}H_{13}N_2O_3$
315	$C_{20}H_{15}N_2O_3$
316	$C_{20}H_{16}N_2O_2$
332	$C_{20}H_{16}N_2O_3$

Nevertheless, the mass spectrum of the [[H3LCdCl2].2H2O] complex (4) exhibited a molecular ion peak at m/z 552 amu, confirming its formula weight (F.W. 552). The observed mass fragmentation patterns at m/z = 36, 55, 79, 93, 104, 136, 184, 187, 212, 226, 396, 448, 474, and 552 amu correspond to $2H_2O$, C_3H_3O, C_5H_3O, C_6H_5O, C_7H_4O, C_7H_6NO, $CdCl_2$, $C_{11}H_9NO_2$, $C_{13}H_{10}NO_2$, $C_{13}H_{10}N_2O_2$, $C_{13}H_{10}NO_2CdCl_2$, $C_{16}H_{12}N_2O_2CdCl_2$, $C_{18}H_{14}N_2O_2CdCl_2$, and [H3LCdCl$_2$].2H$_2$O moieties, respectively, robustly support the proposed structure of the complex (Table 2, ii).

Table 2 (ii) Mass spectrum of **Cd(II)** complex (**4**)

m/z	Rel. Int.	Fragment
36		$2\ H_2O$
55		C_3H_3O
79		C_5H_3O
93		C_6H_5O
104		C_7H_4O
136		C_7H_6NO
184		$CdCl_2$
187		$C_{11}H_9NO_2$
212		$C_{13}H_{10}NO_2$
226		$C_{13}H_{10}N_2O_2$
396		$C_{13}H_{10}NO_2CdCl_2$
448		$C_{16}H_{12}N_2O_2CdCl_2$
474		$C_{18}H_{14}N_2O_2CdCl_2$
552		$[H_3LCdCl_2].2\ H_2O$

PROTON NUCLEAR MAGNETIC RESONANCE SPECTRA (^{1}H-NMR)

The ^{1}H-NMR spectra of the ligand in deuterated DMSO exhibited peaks consistent with the proposed structure. Notably, the spectrum featured a chemical shift observed as a singlet at 5.5 ppm (S, H, OH), assigned to the proton of the aromatic hydroxyl group. Additionally, chemical shifts at 7.8 ppm were attributed to the azomethine protons (H-C=N), while the chemical shift appearing as a singlet at 8.1 ppm was assigned to the proton of the NH group. A distinct set of signals appeared as multiples in the 6.8-7.4 ppm range, corresponding to the protons of the aromatic rings (Abu El-Reash et al., 1990).

IR SPECTRA

The bonding mode between the ligand and the metal ions was elucidated by comparing the IR spectra of the ligand and its metal complexes (2-4). The ligand exhibited bands in the 3640-3375-3350-2740 cm⁻¹ ranges, corresponding to the presence of two types of intra- and intermolecular hydrogen bonds involving OH and NH groups with the imine group (Lever and chemistry, 1984). Strong bands at 1640 and 1625 cm⁻¹ were attributed to ν(C═O) and ν(C=N), respectively. A medium band at 3280 cm⁻¹ was assigned to ν(N-H) group (Bosch and Rosich, 2008). The shift of the ν(NH) group in the complexes from the region of the free ligand indicated the involvement of the NH group in metal ion coordination. Bands at 1456, 756, and 1400, 700 cm⁻¹ were assigned to ν(Ar) vibration (Khaled et al., 2013).Comparing the IR spectra of the complexes (2-4) with that of the free ligand revealed bands in the 3615-3501 cm⁻¹ and 3375-3115 cm⁻¹, 3320-3150 cm⁻¹, and 2850-2480 cm⁻¹ ranges, indicating the presence of two types of intra- and intermolecular hydrogen bonds and hydrated water molecules. The shift of the ν(C═N) bands of the imine by 14-24 cm⁻¹ toward lower wavenumbers in the complexes suggested coordination through the nitrogen of the azomethine group (CH═N) (Naskar et al., 2011). This was further supported by the appearance of new bands in the 590-531 cm⁻¹ range, assigned to ν(M-N). Complexes (2-4) displayed a ν(C=O) band at 1665-1622 range, while showing a lower shift of ν(OH), indicating coordination to the metal ion in the protonated form (Mustafa and Satyanarayana, 2010). The aromatic ring vibrations appeared in the 1595-1385 cm⁻¹ and 812-658 cm⁻¹ ranges.The sulphato complex (3) exhibited bands at (1242-1105), (1138-1130), (1095-1050), and (690-655) ranges, assigned to the bidentate sulphate group (El-Tabl, 2002). The chloride complexes (2,4) displayed bands at (466-450 cm⁻¹), attributed to ν(Cl) chloride group. Complexes (2-4) showed bands in the 596-531 cm⁻¹ range assigned to ν(M-N) and bands in the 665-613 cm⁻¹ range were attributed to ν(M-O) (Gliemann, 1978). The detailed IR data are presented in Table 3.

Table 3 IR Frequencies of the Bands (cm^{-1}) of Ligand **[H$_3$L], (1)** and its Metal complexes

No	Compound	v(H$_2$O)	v(OH)	v(H-bonding)	v(NH)	v(C=O)	v(C=N)	v(Ar)	v(SO$_4$),(Cl)	v(M-O)	v(M-N)
(1)	H$_3$L	-	3451,3400, 1294	3640-3375,3350-2740	3280	1640	1625	1456,756,1400,700	-	-	-
(2)	[H$_3$LCuCl$_2$].2 H$_2$O	3475-3310,3300-3090	3448,3395, 1297,1243	3565-3240,3280-2710	3234	1665	1610	1535,752,1480,700	466	665	596
(3)	[H$_3$LAg$_2$(SO$_4$)]	3585-3265,3220-2998	3410,3285, 1300,1238	3615-3305,3300-2465	3258	1644	1602	1498,750,1465,658	1105,1038,1050,690	613	
(4)	[H$_3$LCdCl$_2$].2 H$_2$O	3470-3365,3360-3050	3430,3390, 1243,1301	3560-3210,3200-2620	3225	1622	1601	1500,751,1485,701	450	664	565

ELECTRONIC SPECTRA AND MAGNETIC MOMENTS

The electronic absorption spectral data for the ligand and its metal complexes in DMF are detailed in Table 4. The ligand exhibited three bands at 290, 310, and 315 nm. The first band is likely associated with the $\pi \rightarrow \pi^*$ transition, which remains nearly unchanged upon complexation. However, the second bands corresponded to the n $\rightarrow \pi^*$ and charge transfer transitions of the imine and amide groups (Suvarapu et al., 2012). These bands shifted to lower energy upon complex formation, indicating the involvement of these groups in coordination with the metal ions.The electronic spectra of the copper (II) complex (2) revealed bands at 288, 302, 308, 432, 580, and 600 nm. The first bands are assigned to intraligand transitions, while the other bands are assigned to $^2B_{1g} \rightarrow {}^2A_{1g}$ v_1(dx^2-y^2 $\rightarrow$ dz^2),$^2B \rightarrow {}^2B_{2g}$, $v2$(dx^2-y^2 $\rightarrow$ dxy), and $^2B_{1g} \rightarrow {}^2Eg$, v_3(dx^2-y^2 $\rightarrow$ dxy, dyz) transitions, respectively.These transitions suggest that the copper(II) ion adopts a tetragonally distorted octahedral geometry. This distortion could be attributed to the Jahn-Teller effect acting on the d^9 electronic ground state of the six-coordinate system, elongating one trans pair of coordinate bonds and shortening the remaining four (Smith, 1976). The magnetic moment for the copper(II) complex at room temperature was measured to be 1.7 B.M, indicative of an octahedral geometry (Kivelson and Neiman, 1961).The observed bands for the silver(I) complex (3) and cadmium(II) complex (4) (Table 4) were attributed to intraligand transitions within the ligand and indicated a diamagnetic property

Table 4 The electronic spectra (nm) and magnetic moments (B.M.) for the ligand **[H$_3$L](1),** and its complexes

No.	λ_{max} (nm)	μ_{eff} in B.M.
(1)	290 nm (log $\square$ =3.98), 310 nm (log $\square$ =4.25), 315 nm(log $\square$ =4.3)	-
(2)	288,302, 308,432,580,600	1.70
(3)	285,305,318	Dimag.
(4)	287,305,321	Dimag.

ELECTRON SPIN RESONANCE (ESR)

To gain further insights into the stereochemistry and the nature of the metal-ligand bonding (Mitu et al., 2012), the ESR spectrum of Complex (2) displayed an anisotropic type with g∥ > g⊥ > 2.0023, indicating a distorted octahedral structure with a d(x²-y²) ground state. The G value, which is less than 4.0 (Table 5), suggests significant exchange coupling between Cu(II) ions, a confirmation supported by the magnetic moment value. The g∥/A∥, α², and g∥ values further indicated a distorted octahedral structure with covalent bond character (Zoubi et al., 2012). Additionally, the complex exhibited ß$_1^2$ and ß ^{2} values (Table 5), signifying covalent bond character in-plane and out-plane π bonding (Avaji et al., 2008). The calculated orbital population for the d orbital (a$_d^2$) (Table 5) indicated a d(x²-y²) ground state (Opletalovà et al., 2008).The ESR data are shown in Table (5).

Table 5 ESR data for Cu (II) complex

No.	g∥	g⊥	g$_{iso}$^{a}	A∥ (G)	A⊥ (G)	A$_{iso}$^{b} (G)	G^c	ΔE_{xy}	ΔE_{xz}	K$_⊥^2$	K$_∥^2$	K	K^2	g∥/A∥	α^2	ß^2	ß$_1^2$	-2 ß	a$_d^2$(%)
(2)	2.11	2.03	2.056	105	10	41.7	3.7	18248	22988	0.25	0.3	0.51	0.27	3.11	0.44	0.57	0.68	183.4	78.03%

g$_{iso}$ = (2g⊥ + g∥)/3, b) A$_{iso}$ = (2A⊥ + A∥)/3, c) G= (g∥ - 2)/ (g⊥ - 2)

THERMAL ANALYSES (DTA AND TGA)

The thermal data for the complexes are presented in Tables (6,i) - (6,ii), providing support for the stoichiometric formula, the number of water molecules, and the end products (El-Tabl et al., 2011). Thermogravimetric curves for complexes (3 and 4) are exemplified here. The thermogram of complex (3) [H3LAg$_2$SO$_4$] displayed five-step decompositions. The initial step involved the breaking of H-bondings, marked by an endothermic peak at 48°C. Subsequently, one molecule of the coordinated sulfate group (SO$_4$) was lost endothermically, manifesting a peak at 280°C accompanied by a 14.7% (14.9%) weight loss. The endothermic peak at 330°C indicated the melting point of the complex. The final step, observed

as exothermic peaks in the 385-670°C range with a 42.5% weight loss (Calc 42.1%), signified the complete oxidative decomposition of the complex, resulting in the formation of (Ag$_2$O). The thermogram of complex (4) [H3LCdCl$_2$].2H$_2$O exhibited multiple decomposition steps. The initial step involved the breaking of H-bondings, marked by an endothermic peak at 46°C. In the second step, two molecules of hydrated water were lost endothermically, with a peak at 92°C accompanied by a 6.61% (Calc 6.52%) weight loss. A 13.62% (Calc 13.56%) weight loss, accompanied by an endothermic peak observed at 215°C, was assigned to the loss of two coordinated chloride groups (Cl) (Geary, 1971). The endothermic peak at 395°C referred to the melting point of the complex. The final step observed exothermic peaks in the 665-790°C range with a 28.9% weight loss (Calc 28.69%), indicating the complete oxidative decomposition of the complex, resulting in the formation of (CdO).

Table 6 (i) Thermal analysis of complexes

Compound No. Molecular formula	Temp. (°C)	DTA (peak)		TGA (Wt.loss %)		Assignments
		Endo	Exo	Calc.	Found	
Complex (3)	48	Endo	-			Broken of H-bonding
	280	Endo	-	14.9	14.7	Loss of (SO$_4$)group
	330	Endo	-			Melting point
	385-470-670	-	Exo	42.1	42.5	Decomposition process with the formation of Ag$_2$O

Table 6 (ii) Thermal analysis of complexes

Compound No. Molecular formula	Temp. (°C)	DTA (peak)		TGA (Wt.loss %)		Assignments
		Endo	Exo	Calc.	Found	
Complex (4)	46	Endo	-			Broken of H-bonding
	92	Endo	-	6.52	6.61	Loss of 2 (H$_2$O)hydrated water molecule
	215	Endo	-	13.6	13.62	Loss of 2(Cl)atoms
	395	-	Exo			Melting point
	665-740-790	-	Exo	28.9	28.9	Decomposition process with the formation of CdO

TRANSMISSION ELECTRON MICROSCOPY CHARACTERIZATION (TEM)

The determined average diameter of the particles in the tested complex was found to be 29.02±5.02 nm. Transmission electron microscopy (TEM) samples for the colloidal suspension of the complexes in distilled water were meticulously prepared. Colloids were dropped onto carbon-coated TEM grids, allowing the liquid carrier to evaporate in the air, and subsequently assayed using a JEOL 1230 transmission electron microscope (120 kV) following the methodology(El-Tabl et al., 2009). The results revealed varying values for the tested complexes, with the Cu(II) complex (2) exhibiting the smallest size, followed by the Ag(I) complex (3), and finally the Cd(II) complex (4), as illustrated in figures 2(a,b,c,d,e,f,g,i), 3(a,b,c,d,e,f,g,I,j,k), and 4(a,b,c,d,e,f,g,I,j,k), respectively. The complex particles were observed in nano size, within a diameter range of 1 to 100 nm. Such nanoscale dimensions confer new or enhanced size-dependent properties compared to larger particles of the same material. This offers several advantages, including increased bioavailability, dose proportionality, decreased toxicity, smaller dosage forms (e.g., smaller tablets), and stable dosage forms for drugs that are either unstable or have unacceptably low bioavailability in non-nano particulate forms. Furthermore, the increased surface area of the active agent results in faster dissolution in aqueous environments such as the human body, translating to greater bioavailability, smaller drug doses, reduced toxicity, and minimized fed/fasted variability (Bhat et al., 2015).
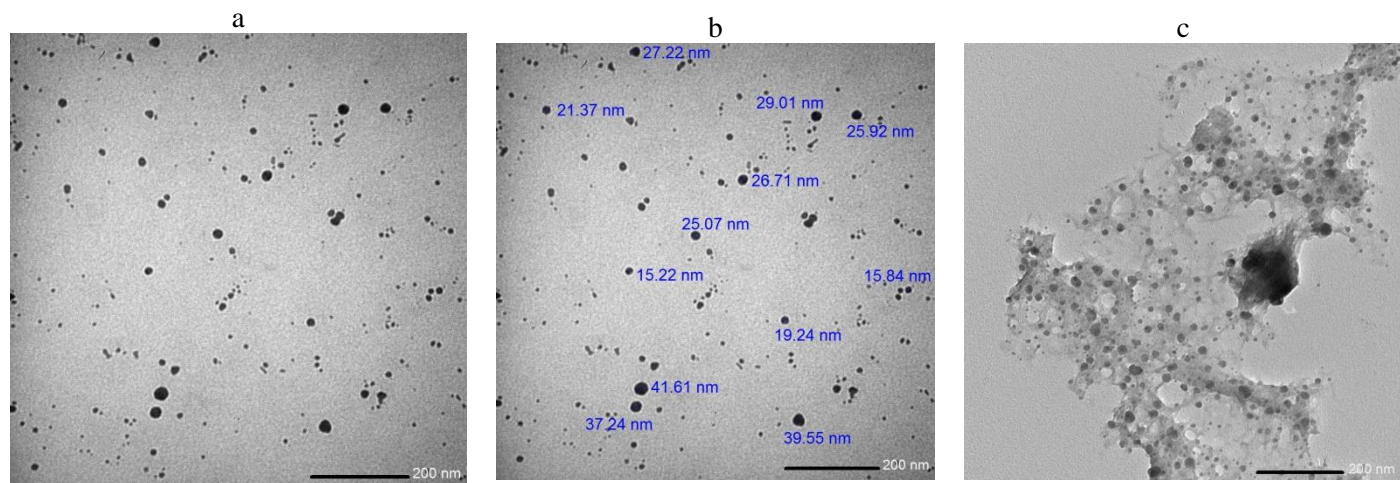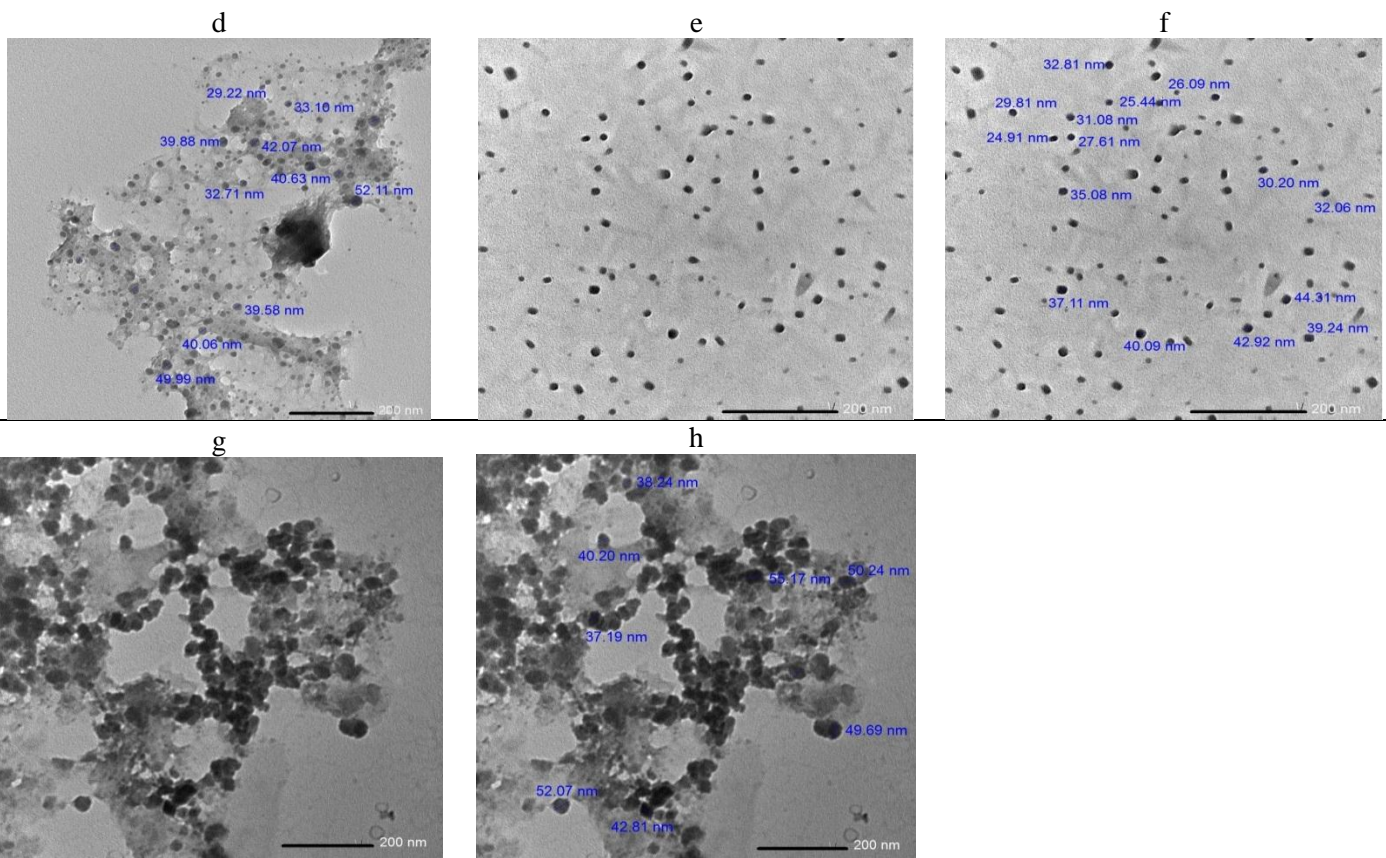
Figure (2) (a,b,c,d,e,f,g,i). TEM images for Cu (II) complex **(2)** nanoparticles
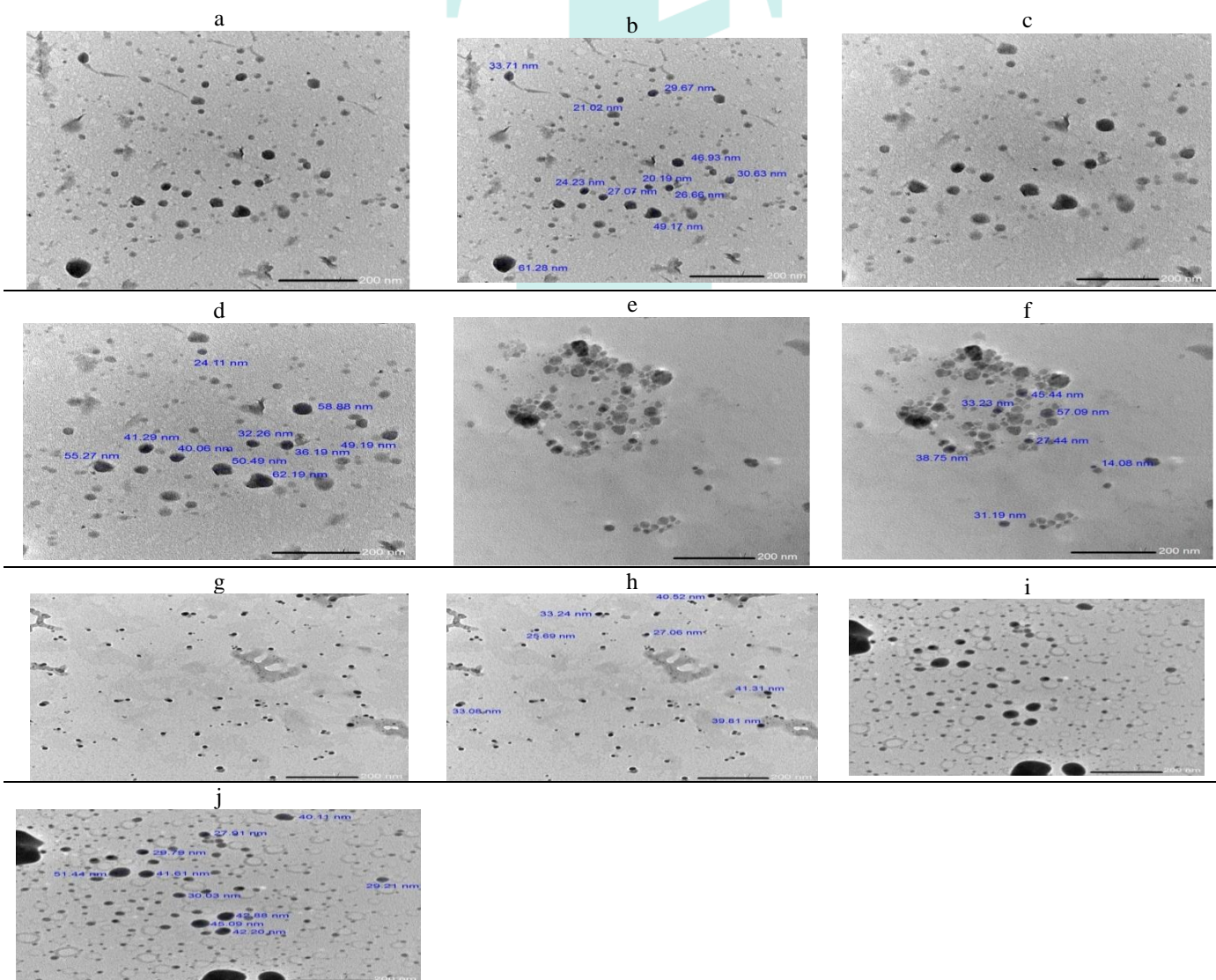
Figure (3) (a,b,c,d,e,f,g,h,I,j). TEM images for Ag(II) complex **(3)** nanoparticles
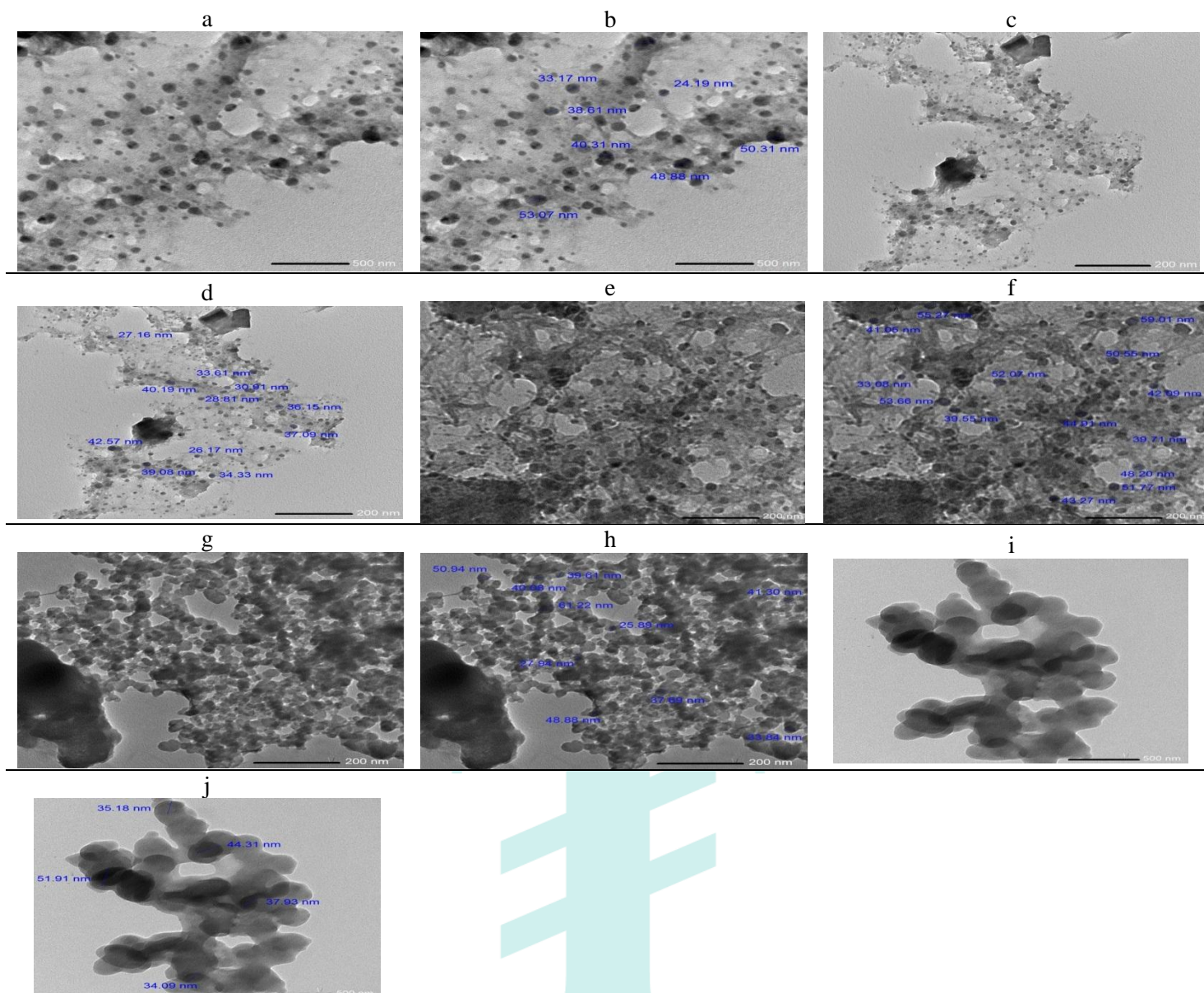
Figure (4) (a,b,c,d,e,f,g,h,I,j)**.** TEM images for Cd (II) complex **(4)** nanoparticles

INVITRO STUDIES
Evaluation of the cytotoxic effect of the tested complex on HepG-2 cell lines by SRB assay

The cytotoxic potential of the ligand H3L (1) and selected metal complexes (2, 3, and 4) was assessed against human liver HEPG cancer cells within a concentration range of 0.25–500 µg/L, as depicted in Figure 5. IC_{50} values were determined for each compound, and the outcomes are presented in Figure 6 and Table 7. Notably, most complexes exhibited significantly higher cytotoxic activities compared to the standard drug Vinblastine Sulfate. The observed cytotoxicity can be attributed to the central metal atom, as explained by Tweedy's chelation theory (El-Tabl et al., 2011). Results indicated distinct cytotoxic values among the tested complexes, with the Ag(I) complex (3) demonstrating the highest potency (IC_{50} = 1.61 µM) against HEPG cancer cells, followed by Cd(II) complex (4) (IC_{50} = 7.72 µM) and Cu(II) complex (2) (IC_{50} = 8.85 µM), while the ligand (1) exhibited the lowest cytotoxicity with an IC_{50} of 22.6 µM.

Additionally, the cytotoxic activity against human breast MCF-7 cancer cells was assessed within the same concentration range, as illustrated in Figure 7. IC_{50} values, depicted in Figure 8 and Table 8, showcased significantly higher cytotoxic activities for most complexes compared to the standard drug Sorafenib (Nexavar). The observed cytotoxicity is attributed to the central metal atom, aligned with Tweedy's chelation theory (Saad El-Tabl et al., 2013). Complex Cu(II) (2) displayed the highest cytotoxicity (IC_{50} = 1.34 µM) against MCF-7 cancer cells, followed by Ag(I) complex (3) (IC_{50} = 3.84 µM). Complex (4) exhibited an IC_{50} of 11.41 µM, while the ligand (1) displayed the lowest cytotoxicity with an IC_{50} of 226 µM. This suggests an enhancement of antitumor activity upon coordination. The positively charged metal increased the ligand's acidity, fostering stronger hydrogen bonds and enhancing biological activity (Feng et al., 2005). Changes in the anion, coordination sites, and metal ion nature significantly influenced biological behavior by altering DNA binding ability (Jarenmark et al., 2010). Metal-mediated hydroxyl radical formation in vivo, analogous to the Fenton reaction, has been suggested to facilitate oxidative tissue injury, as reported by Gaetke and Chow (Elsadek et al., 2017). Evidence for metal-mediated hydroxyl radical formation has been obtained through the ESR-trapping technique(Sayed-Ahmed et al., 2010). Reactive oxygen species are produced via a Fenton-type reaction.

$$LM(II) + H_2O_2 \rightarrow LM(I) + .OOH + H^+$$
$$LM(I) + H_2O_2 \rightarrow LM(II) + .OH + OH^-$$
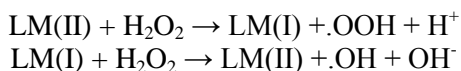
where L, organic ligand

Moreover, the presence of metal introduces a dual impact, acting as a double-edged sword by inducing DNA damage and impeding repair processes (Jayaprakash et al., 2015). Hydroxyl radicals (OH) engage in reactions with DNA sugars and bases, leading to the liberation of free bases and causing strand breaks. Among these reactions, hydrogen atom abstraction from the C4 on the deoxyribose unit is a notable and well-characterized OH reaction, resulting in the formation of sugar radicals and subsequent β-elimination. This mechanism leads to strand breaks and the release of free bases. Solvated electrons represent another mode of attack on DNA bases, likely through a similar reaction mechanism as discussed below for the direct effects of radiation on DNA (Martin et al., 2010).
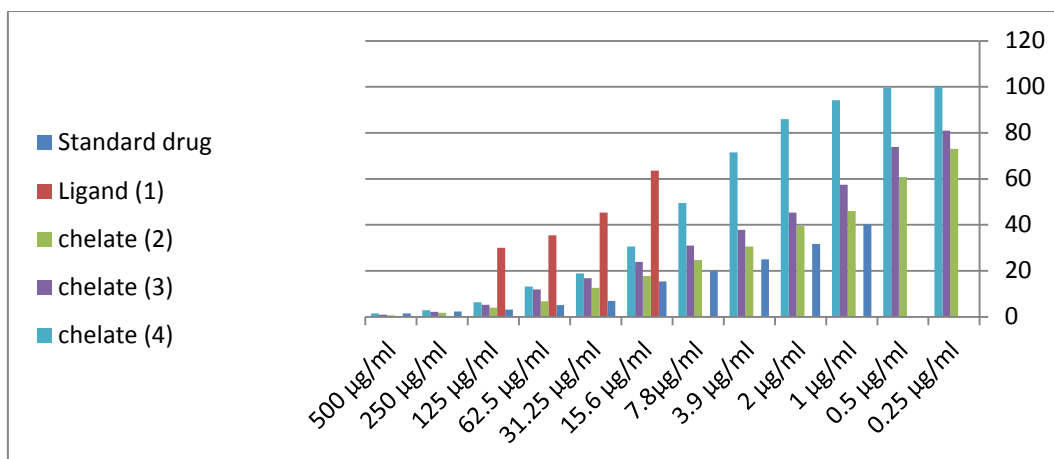
Figure 5 Mean inhibition zone of the ligand(**1**) and metal complexes (**2**), (**3**) and (**4**) against Liver carcinoma HEPG
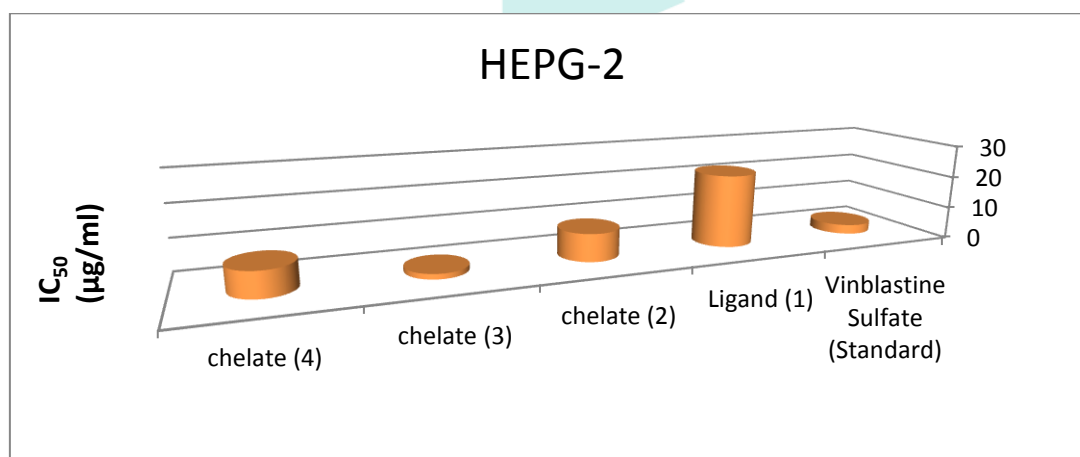
Figure 6 IC$_{50}$ for the the ligand (1) and metal complexes (2), (3) and (4) against Liver carcinoma HEPG
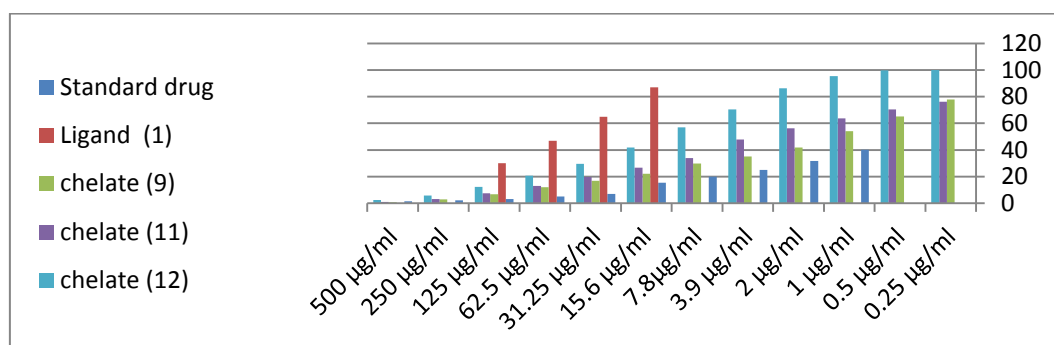
Figure 7 Mean inhibition zone of the ligand (1) and metal complexes (2), (3) and (4) against breast carcinoma MCF-7
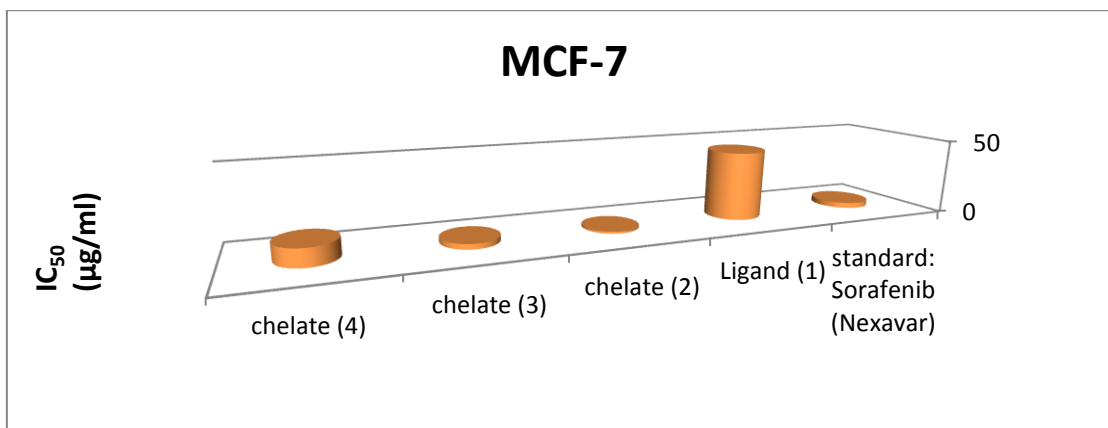
Figure 8 IC$_{50}$ for the the ligand (1) and metal complexes (2), (3)) and (4) against breast carcinoma MCF-7

Table 7 Cytotoxic activity (IC$_{50}$) of the ligand and some metal complexes against human liver HEPG-2

Compound No.	Compound	(IC$_{50}$) HepG-2/ml)
Standard	Vinblastine Sulfate	2.93
Ligand (1)	[H$_3$L]	22.6
Complex (2)	[H3L1CuCl$_2$].2 H$_2$O	8.65
Complex (3)	[H3L1Ag$_2$(SO$_4$)]	1.61
Complex (4)	[H3L1CdCl$_2$].2 H$_2$O	7.72

Table 8 Cytotoxic activity (IC$_{50}$) of the ligand and some metal complexes against human breast MCF-7

Compound No.	Compound	(IC$_{50}$) MCF-72/ml)
Standard	Sorafenib (Nexavar)	3.61
Ligand (1)	[H$_3$L]	226
Complex (2)	[H3L1CuCl$_2$].2 H$_2$O	1.34
Complex (3)	[H3L1Ag$_2$(SO$_4$)]	3.48
Complex (4)	[H3L1CdCl$_2$].2 H$_2$O	11.41

HepG2 cells non-treated (control) 1

HepG2 cells non-treated (control) 2

HepG2 cells non-treated (control) 3

(at conc. 500 µg/ml)

(at conc. 125 µg/ml)

(at conc. 31.25 µg/ml)

(at conc. 7.8 µg/ml)

(at conc. 2 µg/ml)

(at conc. 0.5 µg/ml)
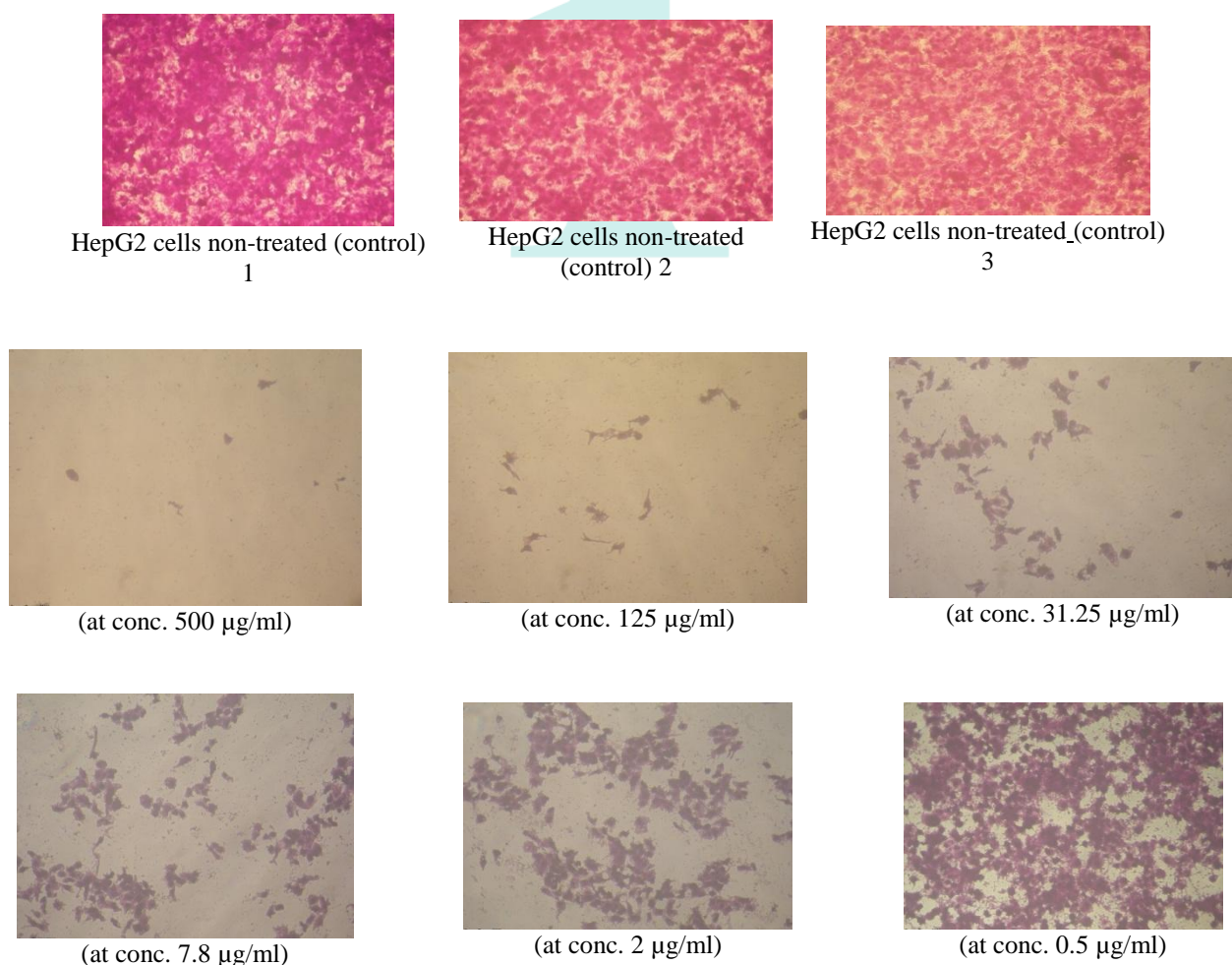
HepG2 cells treated with complex **(2)** after 24h treatment

Figure (9,a) Histograms of cytotoxicity of control HepG2 and some tested complexes

(at conc. 500 μg/ml)

(at conc. 125 μg/ml)

(at conc. 31.25 μg/ml)

(at conc. 7.8 μg/ml)

(at conc. 2 μg/ml)

(at conc. 0.5 μg/ml)
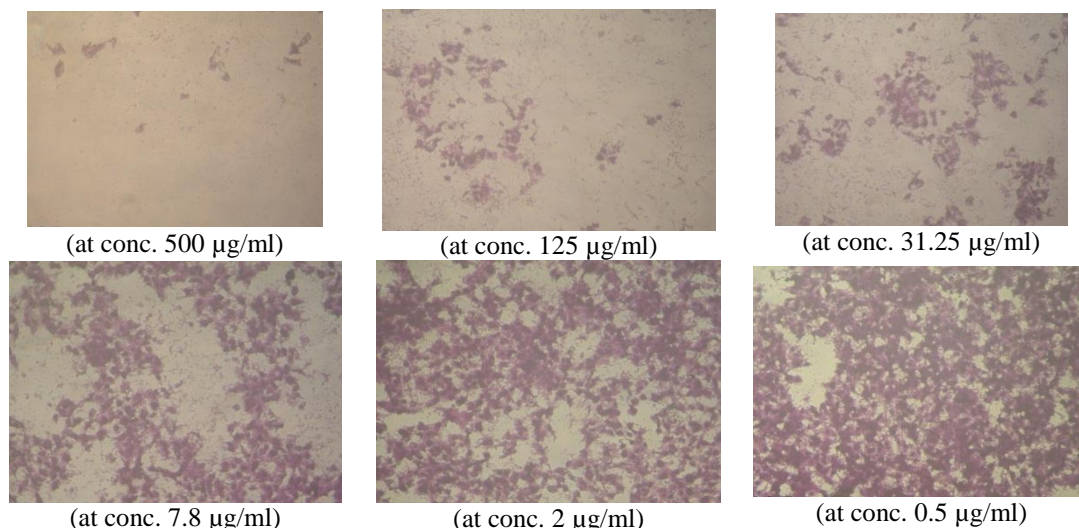
HepG2 cells treated with sample complex **(3)** after 24h treatment

Figure (9,b): Histograms of cytotoxicity of control HepG2 and some tested complexes

(at conc. 500 μg/ml)

(at conc. 125 μg/ml)

(at conc. 31.25 μg/ml)

(at conc. 7.8 μg/ml)

(at conc. 2 μg/ml)

(at conc. 0.5 μg/ml)
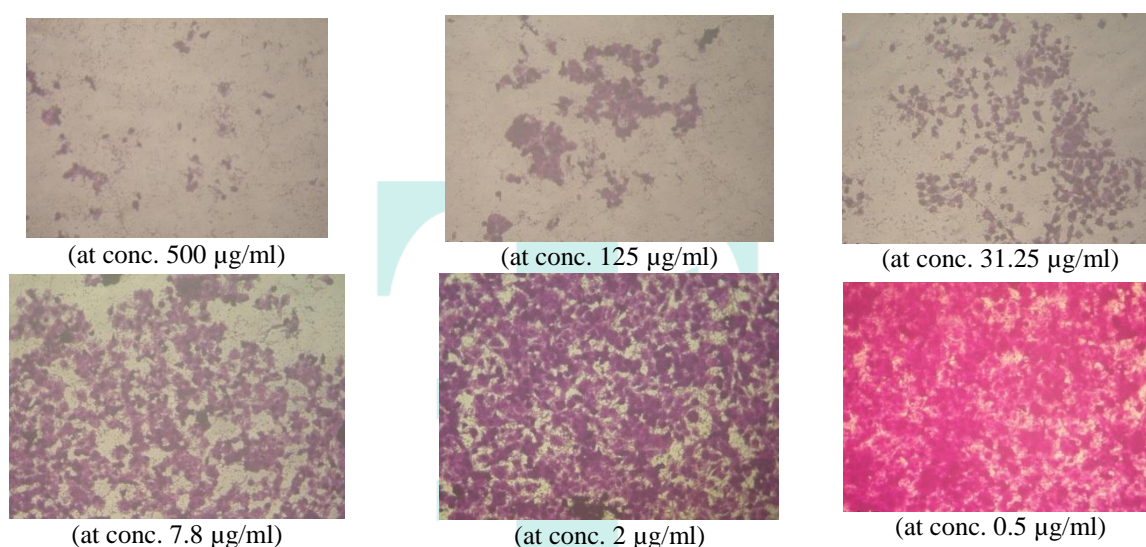
HepG2 cells treated with complex **(4)** after 24h treatment

Figure (9,c): Histograms of cytotoxicity of control HepG2 and some tested complexes

Based on the histogram in Figure 9 (a, b, c), the following observations were made:

1. A reduction in the count of viable cells.
2. Substantial degenerative alterations, including irregularities in cell membrane structure, opacity, poorly defined chromatin organization, cytoplasmic swelling, and optatitic changes. Some cells exhibited characteristics such as shrunken morphology, increased eosinophilia, and picnotic nuclei.
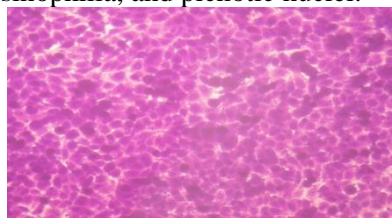
MCF-7 cells non-treated **(control)**

(at conc. 500 μg/ml)

(at conc. 125 μg/ml)
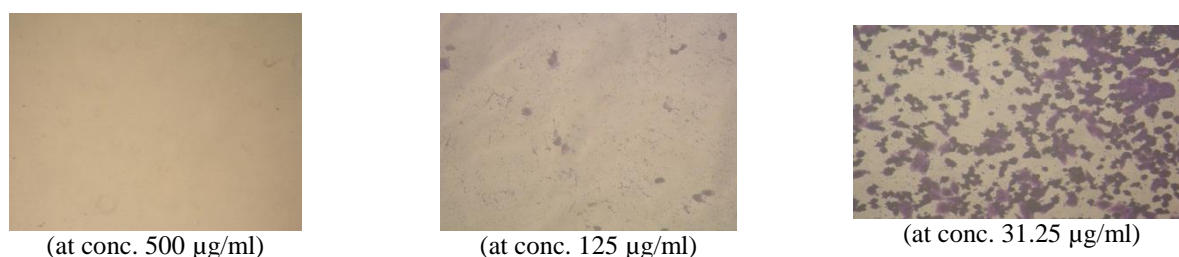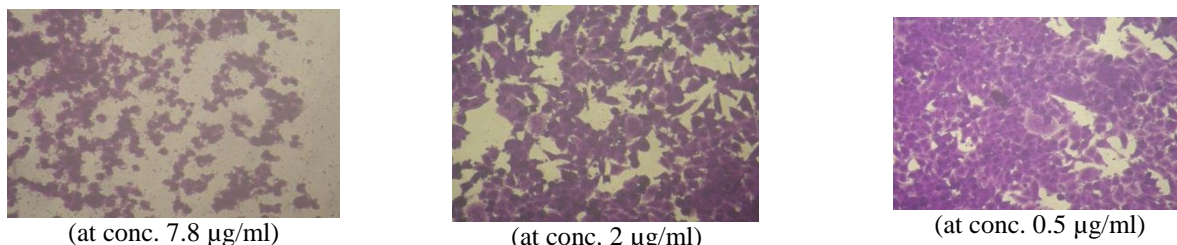
(at conc. 31.25 μg/ml)

(at conc. 7.8 µg/ml)

(at conc. 2 µg/ml)

(at conc. 0.5 µg/ml)

MCF-7 cells treated with sample complex **(2)** after 24h treatment

Figure (10, a): Histograms of cytotoxicity of control **MCF-7** cells non-treated and some tested complexes
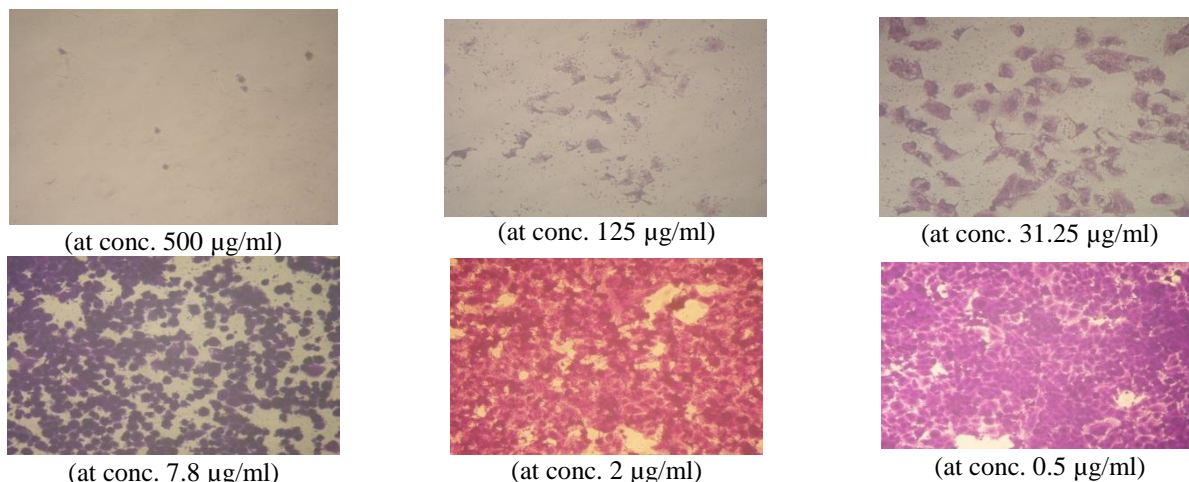
(at conc. 500 µg/ml)

(at conc. 125 µg/ml)

(at conc. 31.25 µg/ml)

(at conc. 7.8 µg/ml)

(at conc. 2 µg/ml)

(at conc. 0.5 µg/ml)

MCF-7 cells treated with complex (3) after 24h treatment

Figure (10, b): Histograms of cytotoxicity of control MCF-7 cells non-treated and some tested complexes

Based on the histogram in Figure 10 (a, b), the following observations were made:

1. A reduction in the count of viable cells.
2. Substantial degenerative changes were noted, characterized by irregular cell membrane structure, opacity, poorly formed chromatin, swelled cytoplasm, and optatitic alterations. Some cells exhibited characteristics such as shrunken morphology, increased eosinophilia, and picnotic nuclei.

IN VIVO STUDIES
Toxicity Study
Toxicity assessments were conducted for the copper(II) complex (2) and silver(I) complex (3) with molecular weights of 501 and 642, respectively. The chemical formulas for these complexes are [H3LCuCl$_2$].2H$_2$O and [H3LAg$_2$(SO$_4$)]. The complexes were dissolved in DMSO and subsequently diluted with sterile saline (0.9% NaCl) to achieve a maximum concentration of 0.2% by volume, facilitating intra-peritoneal injection.

Animals
Forty-nine healthy male albino rats, each 8 weeks old and weighing approximately 180 ± 5 g, were procured from the National Cancer Institute in Cairo, Egypt. The rats were accommodated in cages within a controlled environment with a temperature range of 22-25 °C. They were subjected to adequate ventilation and maintained under a 12-hour light/12-hour darkness cycle, with lights on from 06:00 to 18:00. The rats were provided with a standard laboratory diet consisting of 60% ground cornmeal, 10% bran, 15% ground beans, 10% corn oil, 3% casein, 1% mineral mixture, and 1% vitamin mixture, obtained from Meladco Feed Company in Obour City, Cairo, Egypt. Additionally, the rats had unrestricted access to water throughout the experimental period.

Acute Toxicity Study
The determination of the lethal dose 50 (LD$_{50}$) using experimental animals is a customary practice in drug screening, representing an initial step in the evaluation of a substance's toxic characteristics (Akhila et al., 2007). The acute intra-peritoneal toxicity of the selected complexes was assessed using 21 animals, with 7 animals per group. The complexes were dissolved in DMSO and then diluted with sterile saline 0.9% NaCl to achieve a maximum concentration of 0.2% by volume, enabling intra-peritoneal injection. Administered in graded doses ranging from 1×10-6 to 1×10-4 mmole/L/Kg body weight, the chosen complexes were observed for toxic effects under consistent environmental conditions. The evaluation of toxicological effects, including mortality, was conducted 24 hours after the administration of the chosen complex concentrations and expressed as the lethal dose 50 (LD$_{50}$).

Experimental Design
Twenty-eight animals underwent a 10-day adaptation period before being randomly assigned to four equal groups, each consisting of 7 rats. The animal groups were designated as follows:

Group 1 (Control): Normal, healthy animals received intra-peritoneal injections of a 0.2% solution of DMSO dissolved in
sterile 0.9% NaCl saline for a duration of 6 weeks.

Group 2: Each animal in this group received intra-peritoneal injections of cupper (II) complex (2) at a concentration of
1×10^{-5} mmole/L for the duration of 6 weeks.

Group 3: Each animal in this group received intra-peritoneal injections of Silver (I) complex (3) at a concentration of
1×10^{-5} mmole/L for the duration of 6 weeks.

Blood collection: At the conclusion of the experimental period, animals were subjected to overnight fasting prior to
dissection under light isoflurane anesthesia. Blood was collected from the vena cava and centrifuged at 3000g for 10
minutes; whole EDTA blood was obtained for hematological studies.

Biochemical Analyses: Liver enzyme activities, including aspartate aminotransferase (AST) and alanine aminotransferase
(ALT), were assessed using kinetic kits from Human Diagnostic Kits, Germany (Serag et al., 2019). Liver functions, such
as albumin concentration, and kidney functions, represented by blood urea and serum creatinine, were measured using
Diamond Diagnostic kits, Egypt(Moustafa et al., 2023). All biochemical analyses were conducted using a Biosystems
BTS-350 Spectrophotometer.

Hematological Analyses: Hemoglobin (Hb) levels were determined using Drabkin's solution (Whitehead Jr et al., 2019),
while red blood corpuscle count (RBCs), total leukocyte count (TLC), and platelet count (PLTs) were determined
manually (Abbasi et al., 2021).

Statistical Analysis: Data underwent statistical significance tests using one-way analysis of variance (ANOVA), followed
by Duncan's multiple range test. The statistical analysis was performed using SPSS 20.00 software. Results were
expressed as mean $\pm$ SD, and differences were considered significant at $P \leq 0.05$ (Love et al., 2019).

RESULTS AND DISCUSSION
Biological Studies "In vivo Studies

The LD_{50} for all tested complex nanoparticles demonstrated no toxicity in rats when administered at different doses via
the intra-peritoneal route (Akhila et al., 2007).

Biochemical Analyses
The results presented in Table 9 and Figures 11, 12, 13, 14 indicate that measurements of liver functions (AST, ALT, and
albumin) and renal functions (B. Urea & S. Creatinine) showed no significant differences between the treated groups with
the chosen complexes and the control group. This suggests that the tested complexes have no toxic side effects.

Table 9 Statistical analysis (ANOVA) for liver and kidney function tests in the different groups

Parameters	Control	Complex Cu	Complex Ag
AST (U/l)	87.635±12.152	90.091±18.712	85.183±15.390
ALT (U/l)	40.188±6.967	38.667±9.581	41.857±4.085
Alb (g/dl)	4.212±0.968	4.300±0.691	4.301±0.869
B. Urea (mg/dl)	33.109±3.337	31.127±2.691	30.698±4.697
S. Creatinine (mg/dl)	0.525±0.105	0.601±0.119	0.591±0.168

ANOVA: analysis of variance; AST: aspartate aminotransferase; ALT: alanine aminotransferase; Alb: albumin; B. Urea: Blood urea;
S. Creatinine: Serum creatinine. Each value is represented as mean $\pm$ SD. SD: standard deviation. Data with different superscripts are
significantly different at $p \leq 0.05$
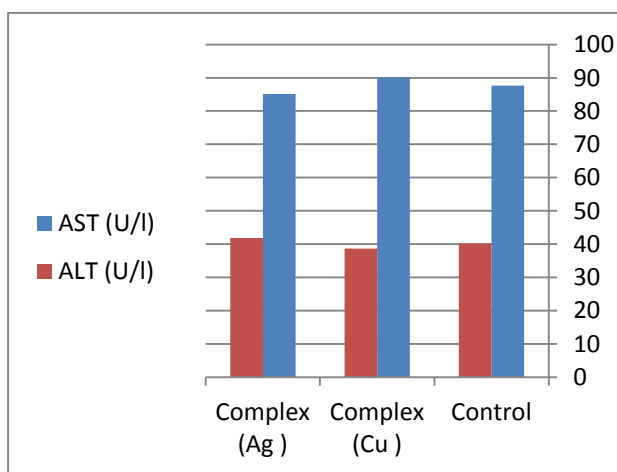
Figure 11 AST and ALT activities in the different groups
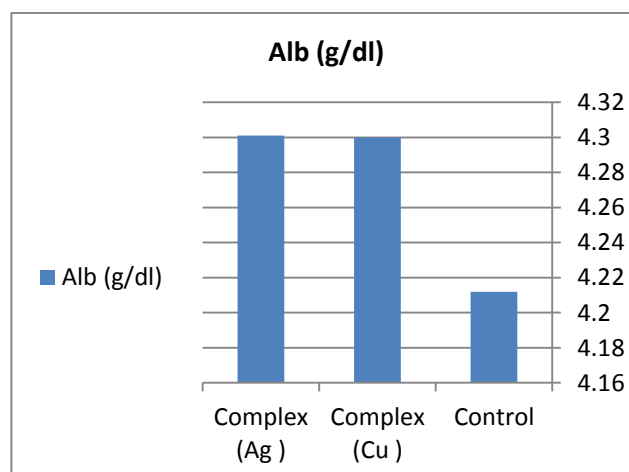
Figure 12 Albumin concentrations in the different groups
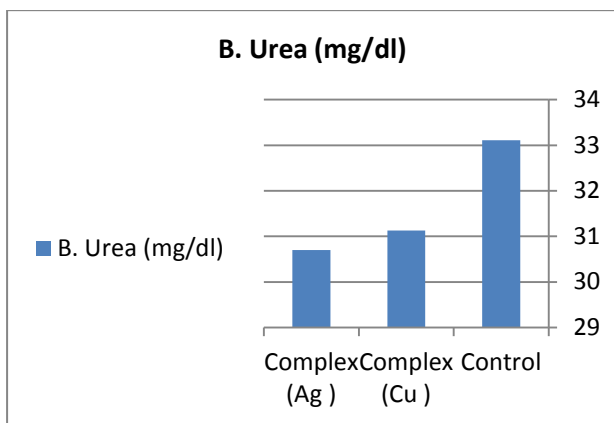
Figure 13 B. Urea concentrations in the different groups
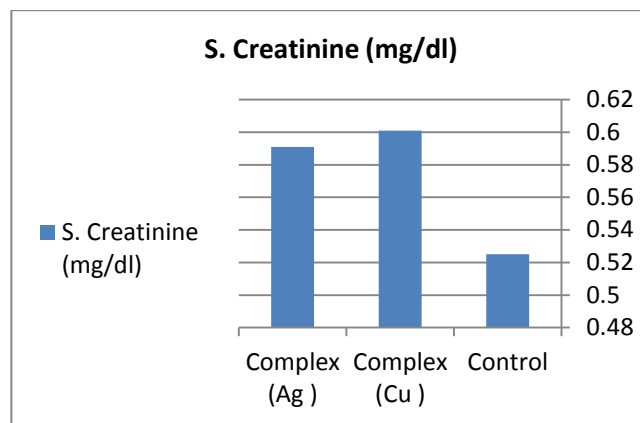
Figure 14 S. Creatinine concentrations in the different groups

Hematological Analysis

Hematological analysis revealed that the examination of certain hematological parameters, including Hemoglobin (Hb), Red Blood Cell count (RBCs), Total Leukocyte Count (TLC), and platelet counts, exhibited no noteworthy alterations when comparing the control group with the groups treated with the selected complexes, as depicted in Table 10 and Figures 15, 16, 17, and 18.

Table 10 Statistical analysis (ANOVA) for hematological tests in the different groups

Parameters	Control	Complex Cu	Complex Ag
Hb (g/dl)	15.940±2.552	16.022±3.698	15.671±3.059
RBCs (X 10^6/cmm)	5.724±1.224	5.827±1.016	5.551±1.016
TLC (X 10^3/cmm)	11.321±3.141	9.367±3.661	10.994±3.357
PLTs (X 10^3/cmm)	619.04±39.218	588.274±59.982	664±28.884

ANOVA: analysis of variance; Hb: Hemoglobin concentration; RBCs: Red blood corpuscles count; T.L.C: Total leucocytic cont; PLT: Platelets count. Each value is represented as mean ± SD. SD: standard deviation Data with different superscripts are significantly different at $p \leq 0.05$
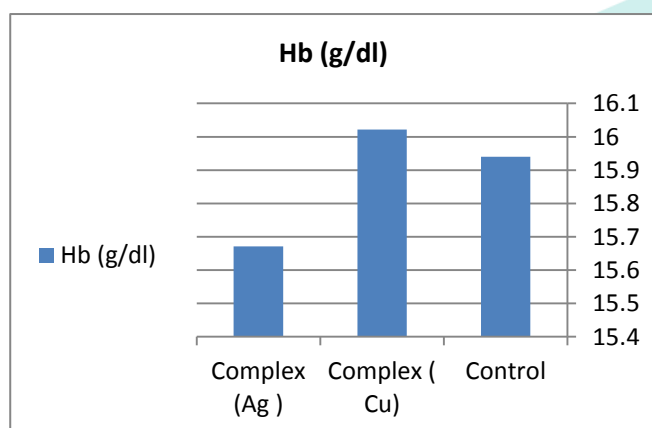
Figure 15 Hemoglobin concentrations in the different groups
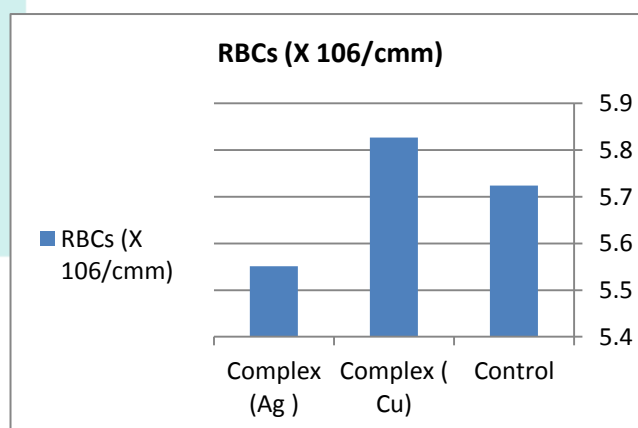
Figure 16 RBCs count in the different groups
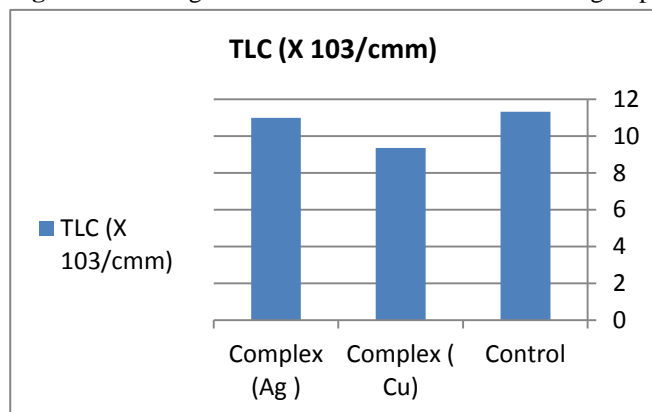
Figure 17 TLC count in the different groups
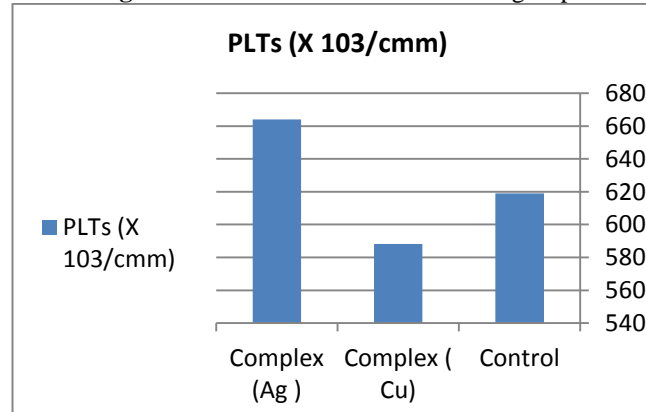
Figure 18 Platelets count in the different groups

Biochemical analyses involved the estimation of liver enzyme activities, including aspartate aminotransferase (AST), alanine aminotransferase (ALT), and alkaline phosphatase (ALP), using kinetic kits obtained from Human Diagnostic Kits, Germany (Serag et al., 2019). Additionally, liver functions, such as albumin concentration, bilirubin (total and

direct), and kidney functions, including blood urea and serum creatinine, were assessed using Diamond Diagnostic kits from Egypt (Moustafa et al., 2023). All biochemical analyses were conducted using a Biosystems BTS-310 Spectrophotometer. The content of malondialdehyde (MDA) was determined (Abbasi et al., 2021).

Hematological analyses included the determination of hemoglobin (Hb) using Drabkin's solution (Whitehead Jr et al., 2019), red blood corpuscle count (RBCs), total leukocytic count (TLC), and platelet count (PLTs), all assessed manually according to the procedure described (Abbasi et al., 2021).

The collective findings from the biochemical and hematological analyses demonstrated no significant differences in the measurements of liver functions, renal functions, and various hematological parameters between the groups treated with the chosen complexes and the control group. This substantiates the absence of toxic side effects associated with the tested complexes.

Hepatocellular Carcinoma Simulation

The three-dimensional (3D) structure of caspase-9 was obtained from the PDB database to serve as the receptor or target protein for molecular docking studies. The interactions of caspase-9 with the amino acids of the active sites of selected proteins associated with hepatocellular carcinoma were explored through molecular docking.

The docked (complex 2) structures, as depicted in figures 19 and 20, exhibited effective ligand-receptor interaction distances generally ≤ 3.5 Å. This observation indicates the presence of typical real bonds, suggesting a high binding affinity. Notably, the closest interaction involved H-donors with caspase-9 at a distance of 3.26 Å in the case of (complex 2), accompanied by a scoring energy (S) of -1.51 kcal. Additionally, (complex 2) demonstrated binding to eight different amino acids (Leu 407(B), Lys 322(A), Asn 405(B), Phe 406(B), and Pro 383(B)), highlighting its potential for effectively inhibiting hepatocellular carcinoma.
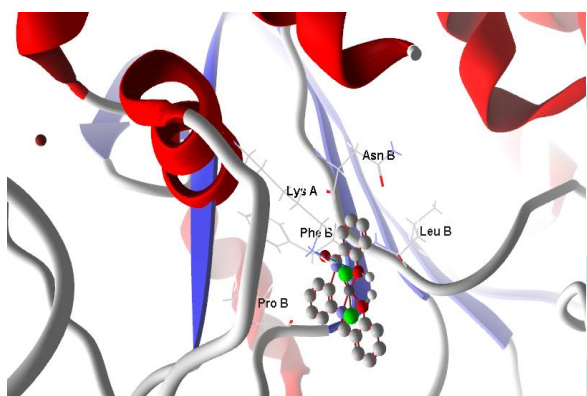
Figure 19 Virtual Molecular docking of the best docked (complex 2) with caspase-9
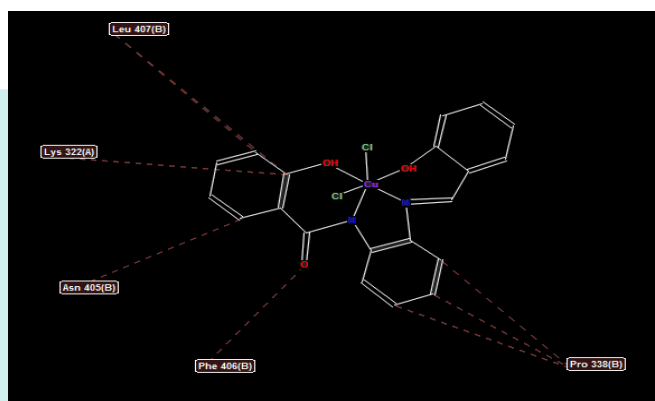
Figure 20 2D structure of Molecular docking of (complex 2) with caspase-9

While examining the docked structures of (complex 3) as illustrated in figures 21 and 22, it was observed that effective ligand-receptor interaction distances were generally ≤ 3.5 Å in most cases. This suggests the presence of typical real bonds, indicating a high binding affinity. For instance, the closest interaction involved H-donors with caspase-9 at a distance of 3.30 Å in the case of (complex 3), accompanied by a scoring energy (S) of -1.49 kcal. Moreover, (complex 3) demonstrated binding to five different amino acids (Lys 280(B), Ile 341(B), Phe 267(B), and Val 264(B)), underscoring its potential for effective inhibition.
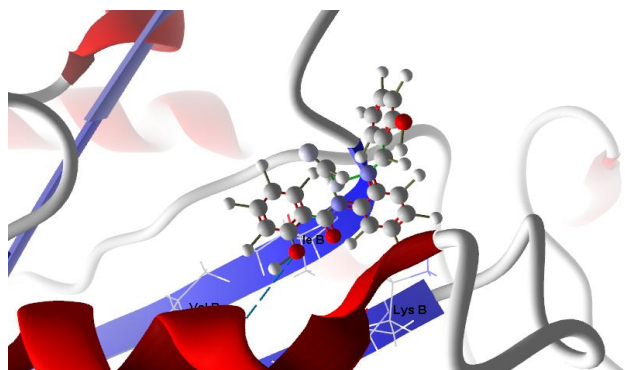
Figure 21 Virtual Molecular docking of the best docked (complex 3) with caspase-9
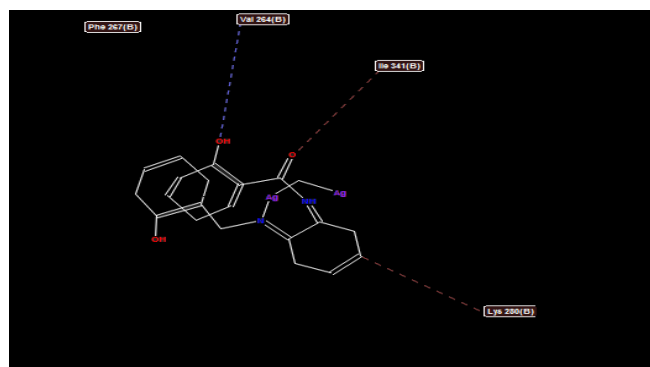
Figure 22 2D structure of Molecular docking of (complex 3) with caspase-9

Upon scrutinizing the docked structures of (complex 4) as depicted in figures 23 and 24, it was observed that effective ligand-receptor interaction distances were mostly ≤ 3.5 Å. This signifies the presence of typical real bonds, indicating a high binding affinity. Notably, the closest interaction involved H-donors with caspase-9 at a distance of 3.25 Å in the case of (complex 4), accompanied by a scoring energy (S) of -1.11 kcal. Additionally, (complex 4) demonstrated binding to

eight different amino acids (Met 400(B), Ser 242(B), Cys 239(B), Pro 247(B), Ala 241(B), Tyr 345(B), Phe 404(B), and Gln 363(A)), highlighting its potential for effective inhibition.
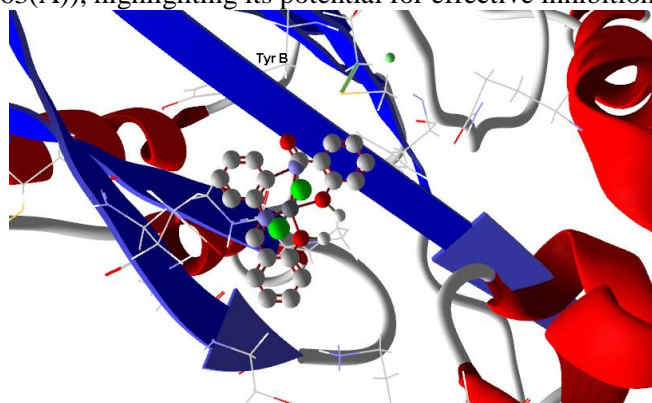
Figure 23 Virtual Molecular docking of the best docked (complex 4) with caspase-9
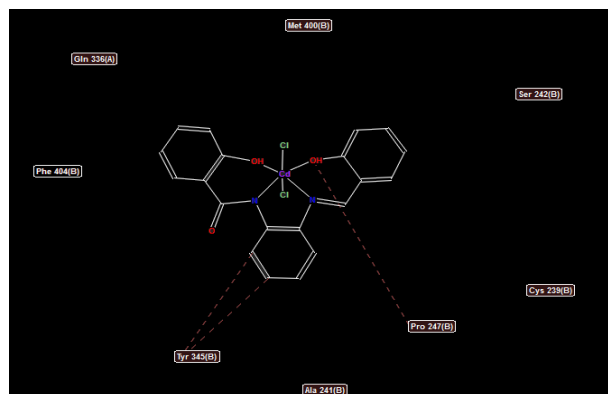
Figure 24 2D structure of Molecular docking of (complex 4) with caspase-9

Breast Cancer Simulation

The crystal structure of human placental aromatase enzyme (protein 3s7s) was chosen to simulate the interaction with potential biologically active compounds. This computational approach provides insights into the ligand-receptor site and the types of interactions, offering an estimation of the distance between the ligand and the receptor within the interaction grid. The scoring energy from docking calculations reflects the degree of inhibitory effect of the ligands. In this study, protein 3s7s represents the aromatase enzyme involved in estrogen synthesis, contributing to estrogen-dependent breast cancer. All ligands exhibited substantial interactions with the receptor protein, as indicated by the scoring energy, showcasing their potential to inhibit 3s7s protein. The docked (complex 2) shown in figures 25 and 26 demonstrated effective ligand-receptor interaction distances mostly ≤ 3.5 Å, indicating the presence of typical real bonds and a high binding affinity. Notably, the closest interaction involved H-donors with 3S7S at a distance of 2.86 Å for (complex 2), accompanied by a scoring energy (S) of -1.17 kcal. Furthermore, nine binding sites involving different amino acids (Gln 218, Phe 221, Asp 222, His 480, and Gly 483) were observed for complex 2, underscoring its potential for high inhibition against breast cancer.
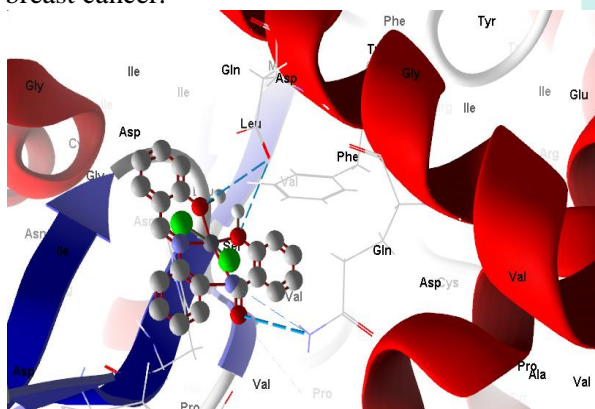
Figure 25 Virtual Molecular docking of the best docked (complex 2) with 3s7s
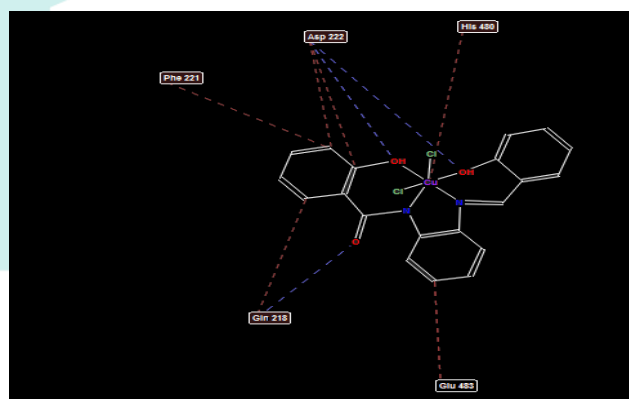
Figure 26 2D structure of Molecular docking of (complex 2) with 3s7s protein

While the docked (complex 3), as depicted in figures 27 and 28, exhibited effective ligand-receptor interaction distances mostly ≤ 3.5 Å, indicating the presence of typical real bonds and thus a high binding affinity. Notably, the closest interaction involved H-donors with 3S7S at a distance of 3.11 Å for (complex 3), accompanied by a scoring energy (S) of -2.40 kcal. Moreover, complex 3 demonstrated fourteen binding sites involving different amino acids (Asp 222, Asp 309, Glu 483, His 480, Gln 218, and Arg 192), highlighting its potential for high inhibition against breast cancer.
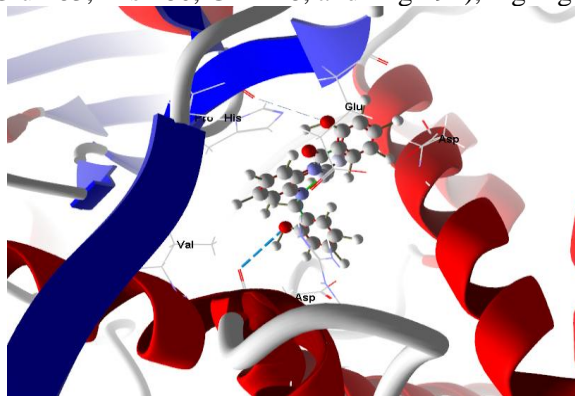
Figure 27 Virtual Molecular docking of the best docked (complex 3) with 3s7s
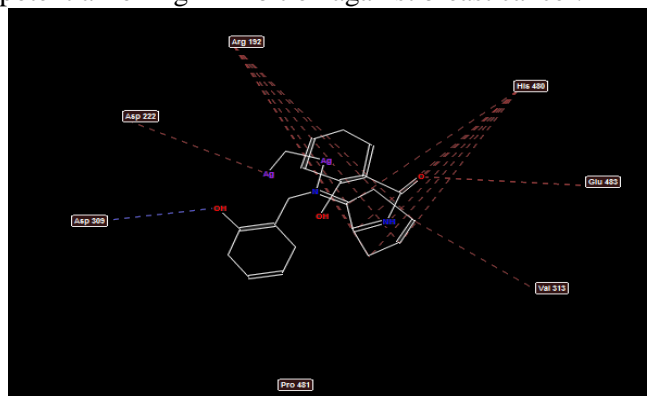
Figure 28 2D structure of Molecular docking of (complex 3) with 3s7s protein

Nevertheless, the docked (complex 4) shown in figures 29 and 30 demonstrated effective ligand-receptor interaction distances mostly ≤ 3.5 Å, suggesting the presence of typical real bonds and thus a high binding affinity. Notably, the closest interaction involved H-donors with 3S7S at a distance of 2.85 Å for (complex 4), along with a scoring energy (S) of -1.21 kcal. Additionally, complex 4 revealed ten binding sites encompassing different amino acids (Phe 221, Glu 483, His 480, Asp 222, and Gln 218), emphasizing its potential for high inhibition against breast cancer.
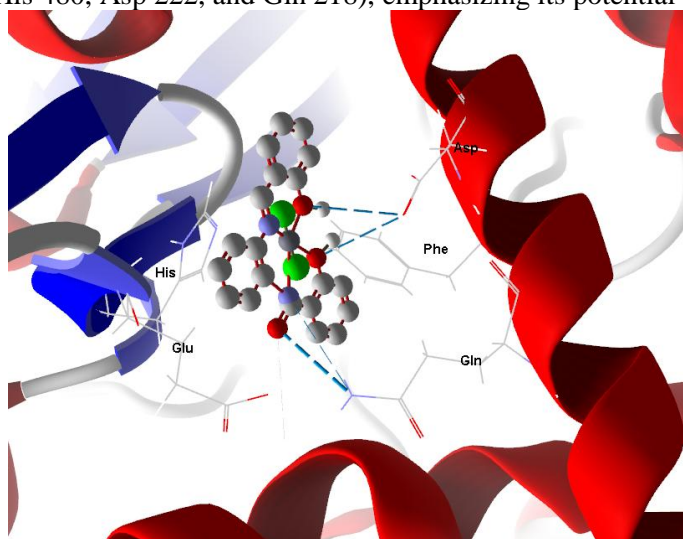
Figure 29 Virtual Molecular docking of the best docked (complex 4) with 3s7s
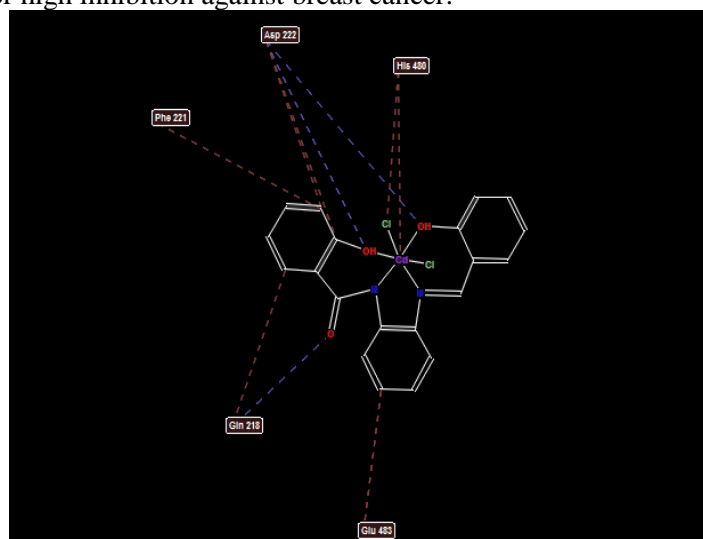
Figure 30 2D structure of Molecular docking of (complex 4) with 3s7s protein

CONCLUSIONS

In this investigation, novel metal complexes derived from (E)-2-hydroxy-N-(2-((2-hydroxybenzylidene)amino)phenyl)benzamide were synthesized. The structural and spectroscopic analyses revealed a tridentate coordination for the ligand, while the metal complexes exhibited a tetragonal distorted octahedral geometry around the metal ions. Molar conductance measurements indicated non-electrolytic behavior for all the complexes. The ligand formed a six-membered ring, incorporating the metal ions in its coordination to the central metal ion.The antitumor activities of both the ligand and some of its metal complexes were evaluated. The toxicity of the ligand and metal complexes was found to be concentration-dependent, with a decrease in cell viability observed as the concentration of complexes increased.

REFERENCES

1. Abbasi, S. Y., Kausar, R., Naz, H. & Chiragh, S. Effect of *Carica papaya* leaf juice on blood cell count of busulfan-induced chronic bone marrow aplasia in mice. Proceedings, 2021. 30-35.
2. Abu El-Reash, G. M., Ibrahim, K. M. & Bekheit, M. M. J. T. M. C. 1990. Ligational behaviour of biacetylmonoxime nicotinoyl hydrazone (H 2 BMNH) towards transition metal ions. 15, 148-151.
3. Akhila, J. S., Shyamjith, D. & Alwar, M. J. C. S. 2007. Acute toxicity studies and determination of median lethal dose. 917-920.
4. Arnau, J., Lauritzen, C., Petersen, G. E., Pedersen, J. J. P. E. & Purification 2006. Current strategies for the use of affinity tags and tag removal for the purification of recombinant proteins. 48, 1-13.
5. Artacho, J., Ascic, E., Rantanen, T., Karlsson, J., Wallentin, C.-J., Wang, R., Wendt, O. F., Harmata, M., Snieckus, V. & Wärnmark, K. 2012. Twisted Amide Analogues of Tröger's Base. *Chemistry – A European Journal,* 18, 1038-1042.
6. Avaji, P. G., Patil, S. A. & Badami, P. S. J. T. M. C. 2008. Synthesis, spectral, thermal, solid-state DC electrical conductivity and biological studies of Co (II) complexes with Schiff bases derived from 3-substituted-4-amino-5-hydrazino-1, 2, 4-triazole and substituted salicylaldehydes. 33, 275-283.
7. Bao, G., Mitragotri, S. & Tong, S. J. A. R. O. B. E. 2013. Multifunctional nanoparticles for drug delivery and molecular imaging. 15, 253-282.
8. BASHORE, C. G., Samardjiev, I. J., Bordner, J. & COE, J. W. 2003. Twisted Amide Reduction under Wolff−Kishner Conditions: Synthesis of a Benzo-1-Aza-Adamantane Derivative. *Journal of the American Chemical Society,* 125, 3268-3272.
9. Beilner, D., Kuhn, C., Kost, B. P., Juckstock, J., Mayr, D., Schmoeckel, E., Dannecker, C., Mahner, S., Jeschke, U., Heidegger, H. H. J. J. O. C. R. & Oncology, C. 2020. Lysine-specific histone demethylase 1A (LSD1) in cervical cancer. 146, 2843-2850.
10. Bhat, M. A., Iqbal, M., Al-Dhfyan, A. & Shakeel, F. J. J. O. M. L. 2015. Carvone Schiff base of isoniazid as a novel antitumor agent: nanoemulsion development and pharmacokinetic evaluation. 203, 111-119.

11. Bosch, F. & Rosich, L. J. P. 2008. The contributions of Paul Ehrlich to pharmacology: a tribute on the occasion of the centenary of his Nobel Prize. 82, 171-179.

12. Brown, D. G. & Boström, J. Analysis of Past and Present Synthetic Methodologies on Medicinal Chemistry: Where Have All the New Reactions Gone?

13. Brunton, L. L., Chabner, B. A. & Knollmann, B. C. 2015. *Goodman & Gilman's: The Pharmacological Basis of Therapeutics, 12e.* New York, NY: McGraw-Hill Education.

14. Chakravorty, A. 1974. Structural chemistry of transition metal complexes of oximes. *Coordination Chemistry Reviews,* 13, 1-46.

15. Clayden, J. 2003. Book Review: The Amide Linkage Structural Significance in Chemistry, Biochemistry, and Materials Science. Edited by Arthur Greenberg, Curt M. Breneman and Joel F. Liebman. *Angewandte Chemie-international Edition - Angew Chem Int Ed,* 42, 1788-1789.

16. Correia, I., Adão, P., Roy, S., Wahba, M., Matos, C., Maurya, M. R., Marques, F., Pavan, F. R., Leite, C. Q. F., Avecilla, F. & Costa Pessoa, J. 2014. Hydroxyquinoline derived vanadium(IV and V) and copper(II) complexes as potential anti-tuberculosis and anti-tumor agents. *Journal of Inorganic Biochemistry,* 141, 83-93.

17. Dörr, M. & Meggers, E. Metal complexes as structural templates for targeting proteins.

18. El-Tabl, A. S., El-Bahnasawy, R. M., Shakdofa, M. M. & Hamdy, A. E.-D. A. I. J. J. O. C. R. 2010. Synthesis of novel metal complexes with isonicotinoyl hydrazide and their antibacterial activity. 34, 88-91.

19. El-Tabl, A. S., El-Saied, F. A., Plass, W., Al-Hakimi, A. N. J. S. A. P. A. M. & Spectroscopy, B. 2008. Synthesis, spectroscopic characterization and biological activity of the metal complexes of the Schiff base derived from phenylaminoacetohydrazide and dibenzoylmethane. 71, 90-99.

20. El-Tabl, A. S., Plass, W., Buchholz, A. & Shakdofa, M. M. J. J. O. C. R. 2009. Synthesis, Spectroscopic Investigation and Biological Activity of Metal (ll) Complexes with N2O4 Ligands. 2009, 582-587.

21. El-Tabl, A. S., Shakdofa, M. M. & El-Seidy, A. J. J. O. T. K. C. S. 2011. Synthesis, characterization and ESR studies of new copper (II) complexes of vicinal oxime ligands. 55, 603-611.

22. El-Tabl, A. S. J. T. M. C. 2002. Synthesis and physico-chemical studies on cobalt (II), nickel (II) and copper (II) complexes of benzidine diacetyloxime. 27, 166-170.

23. El Tabl, A., Abdel Wahed, M., El Assaly, M. M. & Ashour, A. J. E. J. O. C. 2021. Nano-organometallic complexes as therapeutic platforms against breast cancer cell lines;(in vitro study). 64, 1627-1637.

24. Elsadek, B., Mansour, A., Saleem, T., Warnecke, A., Kratz, F. J. D. & Disease, L. 2017. The antitumor activity of a lactosaminated albumin conjugate of doxorubicin in a chemically induced hepatocellular carcinoma rat model compared to sorafenib. 49, 213-222.

25. Feng, G., Mareque-Rivas, J. C., Torres Martín De Rosales, R. & Williams, N. H. J. J. O. T. A. C. S. 2005. A highly reactive mononuclear Zn (II) complex for phosphodiester cleavage. 127, 13470-13471.

26. Fessenden, R. & Fessenden, J. 1998. Organic Chemistry 6th Edition, Brooks. Cole Publishing Company.

27. Geary, W. J. J. C. C. R. 1971. The use of conductivity measurements in organic solvents for the characterisation of coordination compounds. 7, 81-122.

28. Gliemann, G. J. B. D. B. F. P. C. 1978. K. Nakamoto: Infrared and Raman Spectra of Inorganic and Coordination Compounds. John Wiley and Sons, New York, Chichester, Brisbane, Toronto 1978. 3. Aufl., XV, 448 Seiten mit 109 Abbildungen und 95 Tabellen. Preis: $31, 15. 82, 1263-1263.

29. Hie, L., Fine Nathel, N. F., Shah, T. K., Baker, E. L., Hong, X., Yang, Y.-F., Liu, P., Houk, K. N. & Garg, N. K. 2015. Conversion of amides to esters by the nickel-catalysed activation of amide C–N bonds. *Nature,* 524, 79-83.

30. Hoyer, D., Cho, H. & Schultz, P. G. J. J. O. T. A. C. S. 1990. New strategy for selective protein cleavage. 112, 3249-3250.

31. Huang, Z., Zhou, J.-K., Peng, Y., He, W. & Huang, C. J. M. C. 2020. The role of long noncoding RNAs in hepatocellular carcinoma. 19, 1-18.

32. Jarenmark, M., Csapó, E., Singh, J., Wöckel, S., Farkas, E., Meyer, F., Haukka, M. & Nordlander, E. J. D. T. 2010. Unsymmetrical dizinc complexes as models for the active sites of phosphohydrolases. 39, 8183-8194.

33. Jayaprakash, R., Ramesh, V., Sridhar, M., Sasikala, C. J. J. O. P. & Sciences, B. 2015. Antioxidant activity of ethanolic extract of Tinospora cordifolia on N-nitrosodiethylamine (diethylnitrosamine) induced liver cancer in male Wister albino rats. 7, S40.

34. Kaspar, A. A. & Reichert, J. M. 2013. Future directions for peptide therapeutics development. *Drug Discov Today,* 18, 807-17.

35. Kemnitz, C. R. & Loewen, M. J. J. J. O. T. A. C. S. 2007. "Amide resonance" correlates with a breadth of C− N rotation barriers. 129, 2521-2528.

36. Khaled, S., Zamir Ahmed, M., Khan, F. G. & Kabeer Ahmed, S. J. I. J. O. I. C. 2013. Synthesis, characterization, and photophysical studies of some novel ruthenium (II) polypyridine complexes derived from benzothiazolyl hydrazones. 2013.

37. Kim, K. E., Li, J., Grubbs, R. H. & Stoltz, B. M. J. J. O. T. A. C. S. 2016. Catalytic anti-Markovnikov transformations of hindered terminal alkenes enabled by aldehyde-selective Wacker-type oxidation. 138, 13179-13182.

38. Kirby, A. J., Komarov, I. V. & Feeder, N. 2001. Synthesis, structure and reactions of the most twisted amide. *Journal of the Chemical Society, Perkin Transactions 2*, 522-529.

39. Kirby, A. J., Komarov, I. V. & Feeder, N. J. J. O. T. A. C. S. 1998a. Spontaneous, millisecond formation of a twisted amide from the amino acid, and the crystal structure of a tetrahedral intermediate. 120, 7101-7102.

40. Kirby, A. J., Komarov, I. V., Wothers, P. D. & Feeder, N. J. A. C. I. E. 1998b. The most twisted amide: structure and reactions. 37, 785-786.

41. Kivelson, D. & Neiman, R. J. T. J. O. C. P. 1961. Esr Studies On The Bonding In Copper Complexes. 35, 149-155.

42. Kosinska, A. D., Moeed, A., Kallin, N., Festag, J., Su, J., Steiger, K., Michel, M.-L., Protzer, U. & Knolle, P. A. J. S. R. 2019. Synergy of therapeutic heterologous prime-boost hepatitis B vaccination with CpG-application to improve immune control of persistent HBV infection. 9, 10808.

43. Lever, A. P. J. S. I. P. & Chemistry, T. 1984. Inorganic electronic spectroscopy. 33.

44. Li, G., Guan, R.-L., Ji, L.-N. & Chao, H. 2014. DNA Condensation Induced by Metal Complexes. *Coordination Chemistry Reviews,* 281.

45. Li, X. & Zou, G. 2015. Acylative Suzuki coupling of amides: acyl-nitrogen activation via synergy of independently modifiable activating groups. *Chemical Communications,* 51**,** 5089-5092.

46. Love, J., Selker, R., Marsman, M., Jamil, T., Dropmann, D., Verhagen, J., Ly, A., Gronau, Q. F., Šmíra, M. & Epskamp, S. J. J. O. S. S. 2019. JASP: Graphical statistical software for common statistical designs. 88**,** 1-17.

47. Martin, R., Menchon, C., Apostolova, N., Victor, V. M., Alvaro, M., Herance, J. R. & Garcia, H. J. A. N. 2010. Nano-jewels in biology. Gold and platinum on diamond nanoparticles as antioxidant systems against cellular oxidative stress. 4, 6957-6965.

48. Meng, G. & Szostak, M. 2015a. General Olefin Synthesis by the Palladium-Catalyzed Heck Reaction of Amides: Sterically Controlled Chemoselective N☐C Activation. *Angewandte Chemie International Edition,* 54**,** 14518-14522.

49. Meng, G. & Szostak, M. 2015b. Sterically Controlled Pd-Catalyzed Chemoselective Ketone Synthesis via N–C Cleavage in Twisted Amides. *Organic Letters,* 17**,** 4364-4367.

50. Meng, G. & Szostak, M. 2016a. Palladium-catalyzed Suzuki–Miyaura coupling of amides by carbon–nitrogen cleavage: general strategy for amide N–C bond activation. *Organic & Biomolecular Chemistry,* 14**,** 5690-5707.

51. Meng, G. & Szostak, M. 2016b. Rhodium-Catalyzed C–H Bond Functionalization with Amides by Double C–H/C–N Bond Activation. *Organic Letters,* 18**,** 796-799.

52. Mitu, L., Ilis, M., Raman, N., Imran, M. & Ravichandran, S. J. J. O. C. 2012. Transition metal complexes of isonicotinoyl–hydrazone-4-diphenylaminobenzaldehyde: synthesis, characterization and antimicrobial studies. 9**,** 365-372.

53. Miyasaka, H., Ieda, H., Re, N., Crescenzi, R. & Floriani, C. 1998. Assembling Bi-, Tri- and Pentanuclear Complexes into Extended Structures Using a Desolvation Reaction: Synthesis, Structure, and Magnetic Properties of Manganese(III)−Schiff-Base−Hexacyanoferrate Polymeric Compounds and Their Derived Extended Structures. *Inorganic Chemistry,* 37**,** 255-263.

54. Moustafa, A. H., Pasha, H. F., Abas, M. A., Aboregela, A. M. J. A. & Biology, C. 2023. The ameliorating role of sofosbuvir and daclatasvir on thioacetamide-induced kidney injury in adult albino rats. 56**,** 109-121.

55. Mujika, J. I., Mercero, J. M. & Lopez, X. J. J. O. T. A. C. S. 2005. Water-promoted hydrolysis of a highly twisted amide: Rate acceleration caused by the twist of the amide bond. 127**,** 4445-4453.

56. Mustafa, B. & Satyanarayana, S. J. J. O. T. K. C. S. 2010. Vitamin B 12 Model Complexes: Synthesis and Characterization of Thiocyanato Cobaloximes and Thiocyanato Bridged Dicobaloximes of O-donor Ligands: DNA Binding and Antimicrobial Activity. 54**,** 687-695.

57. Naskar, S., Naskar, S., Mondal, S., Majhi, P. K., Drew, M. G. & Chattopadhyay, S. K. J. I. C. A. 2011. Synthesis and spectroscopic properties of cobalt (III) complexes of some aroyl hydrazones: X-ray crystal structures of one cobalt (III) complex and two aroyl hydrazone ligands. 371**,** 100-106.

58. Opletalova, V., Kalinowski, D. S., Vejsova, M., Kunes, J., Pour, M., Jampilek, J., Buchta, V. & Richardson, D. R. J. C. R. I. T. 2008. Identification and characterization of thiosemicarbazones with antifungal and antitumor effects: cellular iron chelation mediating cytotoxic activity. 21**,** 1878-1889.

59. Pattabiraman, V. R. & Bode, J. W. Rethinking amide bond synthesis.

60. Radzicka, A. & Wolfenden, R. J. J. O. T. A. C. S. 1996. Rates of uncatalyzed peptide bond hydrolysis in neutral solution and the transition state affinities of proteases. 118**,** 6105-6109.

61. Saad El-Tabl, A., Abd-Elwahed, M., Hemid Mohammed, M. J. C. S. & Bioavailability 2013. Synthesis, spectral characterisation and cytotoxic effect of metal complexes of 2-(2-(4-carboxyphenyl) guanidino) acetic acid ligand. 25**,** 133-146.

62. Sawosz, E., Chwalibog, A., Szeliga, J., Sawosz, F., Grodzik, M., Rupiewicz, M., Niemiec, T. & Kacprzyk, K. J. I. J. O. N. 2010. Visualization of gold and platinum nanoparticles interacting with Salmonella enteritidis and Listeria monocytogenes. 631-637.

63. Sayed-Ahmed, M. M., Aleisa, A. M., Al-Rejaie, S. S., Al-Yahya, A. A., Al-Shabanah, O. A., Hafez, M. M., Nagi, M. N. J. O. M. & Longevity, C. 2010. Thymoquinone attenuates diethylnitrosamine induction of hepatic carcinogenesis through antioxidant signaling. 3**,** 254-261.

64. Schepartz, A. & Cuenoud, B. J. J. O. T. A. C. S. 1990. Site-specific cleavage of the protein calmodulin using a trifluoperazine-based affinity reagent. 112**,** 3247-3249.

65. Schmitz, K. 2010. Amino Acids, Peptides and Proteins in Organic Chemistry. Volume 1 – Origins and Synthesis of Amino Acids. Edited by Andrew B. Hughes. *Angewandte Chemie International Edition,* 49**,** 3717-3718.

66. Serag, H. M., El Komy, M. M. & Ahmed, H. S. J. T. E. J. O. H. M. 2019. Assessment the Role of Bisphenol A on Chemotherapeutic Efficacy of Cisplatin against Hepatocellular Carcinoma in Male Rats. 74**,** 352-363.

67. Shi, S., Meng, G. & Szostak, M. 2016. Synthesis of Biaryls through Nickel-Catalyzed Suzuki–Miyaura Coupling of Amides by Carbon–Nitrogen Bond Cleavage. *Angewandte Chemie International Edition,* 55**,** 6959-6963.

68. Shi, S. & Szostak, M. 2016. Efficient Synthesis of Diaryl Ketones by Nickel-Catalyzed Negishi Cross-Coupling of Amides by Carbon–Nitrogen Bond Cleavage at Room Temperature Accelerated by a Solvent Effect. *Chemistry – A European Journal,* 22**,** 10420-10424.

69. Simon, M. I., Thorner, J., Emr, S. D. & Abelson, J. N. 2000. Applications of chimeric genes and hybrid proteins, Part A: Gene Expression and Protein Purification, Elsevier.

70. Smith, D. J. C. C. R. 1976. Chlorocuprates (ii). 21**,** 93-158.

71. Smith, R. M. & Hansen, D. E. J. J. O. T. A. C. S. 1998. The pH-rate profile for the hydrolysis of a peptide bond. 120**,** 8910-8913.

72. Surati, K. R., Thaker, B. J. S. A. P. A. M. & Spectroscopy, B. 2010. Synthesis, spectral, crystallography and thermal investigations of novel Schiff base complexes of manganese (III) derived from heterocyclic β-diketone with aromatic and aliphatic diamine. 75**,** 235-242.

73. Suvarapu, L. N., Seo, Y. K., Baek, S.-O. & Ammireddy, V. R. J. E.-J. O. C. 2012. Review on analytical and biological applications of hydrazones and their metal complexes. 9**,** 1288-1304.

74. Tani, K. & Stoltz, B. M. J. N. 2006. Synthesis and structural analysis of 2-quinuclidonium tetrafluoroborate. 441**,** 731-734.

75. Vogel, A. I. 1961. Quantitative inorganic analysis including elementary instrumental analysis, Longmans.

76. Wang, B. & Cao, Z. J. C. A. E. J. 2011. Acid-Catalyzed Reactions of Twisted Amides in Water Solution: Competition between Hydration and Hydrolysis. 17**,** 11919-11929.

77. Whitehead Jr, R. D., Mei, Z., Mapango, C. & Jefferds, M. E. D. J. A. O. T. N. Y. A. O. S. 2019. Methods and analyzers for hemoglobin measurement in clinical laboratories and field settings. 1450**,** 147-171.

78. Yogesh, B., Vineeta, B., Rammesh, N. & Saili, P. J. J. O. P. 2016. Biosynthesized platinum nanoparticles inhibit the proliferation of human lung-cancer cells in vitro and delay the growth of a human lung-tumor xenograft in vivo:-In vitro and in vivo anticancer activity of bio-Pt NPs. 19**,** 114.

79. Zoubi, W. A., Kandil, F. & Chebani, M. J. O. C. C. R. 2012. Synthesis of macrocyclic schiff bases based on pyridine-2, 6-dicarbohydrazide and their use in metal cations extraction. 1**,** 2161-0401.1000104.